TECHNICAL REPORT

FOR

NASA Grant NAG-2-541

NASA Technical Monitor: Alex Woo

Report Title:	Radiation and Scattering Analysis of Microstrip Antennas via a Hybrid Finite Element Method
Report Authors:	Jian-Ming Jin and John L. Volakis
Primary University Collaborator:	John L. Volakis
Primary NASA-Ames Collaborator:	Alex Woo
University Address:	The Radiation Laboratory Department of Electrical Engineering and Computer Science The University of Michigan Ann Arbor, MI 48109-2122
Date:	June 1991

Funds for the support of this study have been allocated by the NASA-Ames Research Center, Moffett Field, California, under interchange No. NCA2-543

Table of Contents

FORWARD

This document is the third and last first year progress report of this research project entitled "Scattering by Conformal Antennas and Radomes" funded through the NASA-Ames interchange No. NCA2-543. The following three pages of the report is the executive summary of this year's progress along with an outline of next year's plan. The remaining portion of the report contains two separate papers which should be read in continuum with the first two reports 027723-1-T and 027723-2-T. One of the papers presents an experimental validation of the developed analysis for scattering and input impedance computations, and the other describes a novel model of a resistive sheet within the context of the finite element method.

Background and First Year Progress Summary

The objective of this project is to develop a new technique for analyzing the scattering and radiation properties of planar and conformal microstrip arrays. The proposed technique is a hybrid methodology which combines the finite element and boundary element methods. The resulting system of equations is then solved via the conjugate or biconjugate gradient method and a unique aspect of this solution is the use of the FFT to eliminate the need to generate the boundary element matrix and thus retain the O(n) storage requirement, inherent in the finite element formulation. Consequently, the proposed solution technique is referred to as FE-CGFFT or FE-BGFFT, depending on whether the conjugate or biconjugate gradient method is used to solve the system.

During this year's effort we primarily concentrated on developing the proposed method and associated algorithms for planar arrays of rectangular patches in a filled cavity. Judging from the results presented in this report (027723-3-T) and the two earlier technical reports 027723-1-T and 027723-2-T, the method has proved very successful in all respects and we have exceeded our original goals and expectations outlined in the proposal. Specifically, this year we completed the following subtasks:

1. We implemented the method using new edge-based basis/expansion functions and validated the implementation by comparison with traditional codes based nodal expansion functions. We found that the edge-based expansions, in addition to satisfying the natural corner/edge conditions, lead to faster convergence and are more compatible with the usual boundary element expansion functions.

2. A code was developed with the appropriate input geometry routine to compute the scattering by rectangular patches in a terminated rectangular cavity and rectangular patch arrays also in a cavity filled with substrate material. This implementation relied on brick elements for modeling the cavity volume and rectangular elements at the cavity surface/boundary.

3. Formulations were developed and coded for modeling the antenna input terminals and loads placed at various locations between the patch and the substrate. The effect of the loads was examined and vector maps were generated which demonstrated that most of the field intensity is concentrated near the patch edges. As a result, the scattering pattern was completely dominated by the patches themselves whereas the (shallow) cavity terminations were less important. This observation implies that one could, under certain conditions, neglect the cavity terminations and instead use standard array theory for generating the scattering and radiation patterns of large arrays. Several scattering and radiation patterns were generated which validated this conclusion.

4. A formulation was developed for modeling resistive cards in connection with the standard finite element method. Resistive cards are often used for reducing edge diffraction and are thus important in this implementation. The associated formulation was coded and tested by comparison with a certain physical model of the resistive card.

5. A low cross section body was designed to serve as a platform for measuring the scattering by patch antennas in a cavity. During this year, scattering patterns were measured for single, unloaded, free-standing patches. The measured data were used to validate the proposed formulation and associated code. Good agreement was observed between measurements and calculations in all cases.

6. Input impedance computations were performed using the proposed formulation for a number of patch antennas. This is a first for the finite element method and comparisons were done with calculations based on traditional formulations. Good agreement was observed in all cases in spite of the approximate input terminal model used at this time.

Proposed Work for Second Year

Our primary goals during the second year of this work are

1. To generalize the method for application to circularly conformal arrays. This will involve the development of the finite element formulation using circularly conformal three dimensional elements. These elements must also be conformal to the surface/outer boundary of the cavity and must ensure a convolutional boundary integral to maintain the O(n) storage requirement. Further, the expansion basis for these elements will be developed along with the associated finite and boundary element equations. Essentially, all of the subtasks completed during the first year in connection with the rectangular bricks will be repeated during the second year for the circularly conformal distorted bricks.

2. Improved input antenna feed models will be investigated and developed which account for the presence of the coaxial cable and other possible physical characteristics of the feed.

3. The effect of loads, feed location and structure, resistive card loading and patch geometry will be investigated with respect to the arrays performance parameters.

4. Alternative boundary integral formulations will be investigated which permit conformal modeling of non-rectangular patches without comprising the convolutionality of the operator, essential for maintaining the O(n) storage requirement.

RADIATION AND SCATTERING ANALYSIS OF MICROSTRIP PATCH ANTENNAS VIA A HYBRID FINITE ELEMENT METHOD

Jian-Ming Jin and John L. Volakis

Radiation Laboratory

Department of Electrical Engineering and Computer Science

The University of Michigan

Ann Arbor, Michigan 48109-2122

ABSTRACT

A hybrid numerical technique has been presented in the past for a characterization of the scattering and radiation properties of microstrip patch antennas and arrays residing in a cavity recessed in a ground plane. The technique combines the finite element and boundary integral methods to formulate a system for the solution of the fields at the aperture and those inside the cavity via the biconjugate gradient method in conjunction with the fast Fourier transform (FFT). Numerical results were already presented for scattering and radiation patterns for unloaded and loaded single patches and large arrays. In this report, we present experimental verification of the scattering computations. In addition, input impedance computations are also presented and compared with measurements and calculations based on the moment method.

I. INTRODUCTION

In our previous two technical reports 027723-1-T and 027723-2-T [3], [4], we developed a hybrid finite element formulation for a characterization of the scattering and radiation properties associated with microstrip patch antennas and arrays residing in a cavity that is recessed in a ground plane. The technique employed the finite element method (FEM) to model the substrate in the cavity region and the mesh was terminated at the aperture of the cavity via the boundary integral method. By virtue of the FEM, the analysis is applicable to patch antennas and arrays which reside on or are embedded in the layered dielectric substrate. In an earlier report [4], it was also shown that various feed structures and impedance loads can be modeled within the context of the FEM.

The system resulting from the application of the hybrid finite element - boundary integral method was solved via the biconjugate gradient (BiCG) method in a manner that exploited the sparseness features of the FEM matrix and the convolutional form of the boundary integral. That is, the boundary integral was evaluated via the fast Fourier transform (FFT) and this led to a low $O(N)$ memory demand necessary for large scale implementations. For example, systems with over 120,000 unknowns were handled for scattering and antenna pattern computations and we observed that the employed implementation reached convergence usually within 100 or so iterations. Some scattering and radiation patterns for single patches as well as for large arrays were presented which demonstrated the method's accuracy and capability.

In this final report, we address two important issues. First, an experimental verification is presented for our scattering computations and for this purpose, a low cross section body was designed to serve as a test platform simulating the ground plane. Scattering patterns were measured for single unloaded patches and the measured data

were compared with the computed results and in all cases good agreement was observed between the measurements and calculations. Secondly, we present a number of input impedance computations for the microstrip patch antenna. This is a first for the finite element method and comparisons are presented with measured data and calculations based on traditional formulations. It is shown that in spite of the approximate input terminal model (probe) employed at this time, good agreement was observed between measurements and calculations obtained for the input impedance.

II. SUMMARY OF FORMULATION

Consider the three-dimensional structure illustrated in Figure 1 where a microstrip patch antenna or array is residing on or embedded in a substrate recessed in a ground plane. In accordance with the finite element – boundary integral method [1]-[4], the fields in the cavity can be formulated using the finite element method and those above the antenna can be represented by a boundary integral equation. The two regions are then coupled by enforcing continuity of the tangential fields at the aperture of the cavity.

Let us first formulate the fields inside the cavity via the variational approach which demands that the cavity fields satisfy the variational equation

$$\delta F(\mathbf{E}) = 0 \tag{1}$$

where the functional F is given by

$$\begin{aligned} F(\mathbf{E}) \;=\; & \frac{1}{2}\iiint_V \left[\frac{1}{\mu_r}(\nabla\times\mathbf{E})\bullet(\nabla\times\mathbf{E}) - k_0^2\epsilon_r\mathbf{E}\bullet\mathbf{E}\right] dV \\ & + \iiint_V \left[jk_0Z_0\mathbf{J}^{int}\bullet\mathbf{E} - \frac{1}{\mu_r}\mathbf{M}^{int}\bullet(\nabla\times\mathbf{E})\right] dV \\ & + jk_0Z_0\iint_S (\mathbf{E}\times\mathbf{H})\bullet\hat{\mathbf{z}}\,dS \end{aligned} \tag{2}$$

In this, V represents the cavity volume, S represents the cavity's aperture, and (ϵ_r, μ_r) denote the relative permittivity and permeability of the material filling the cavity. Also,

$k_0 = 2\pi/\lambda$ is the free space wavenumber, $Z_0 = 1/Y_0$ is the free space intrinsic impedance, and $(\mathbf{J}^{int}, \mathbf{M}^{int})$ represent the internal sources in the cavity.

As seen, the surface integral in (2) involves the tangential electric and magnetic fields at the aperture and it is, therefore, necessary that we introduce an additional relation between these fields. This is provided by the boundary integral equation for the fields in the upper half space

$$\mathbf{H}(\mathbf{r}) = \mathbf{H}^{inc}(\mathbf{r}) + \mathbf{H}^{ref}(\mathbf{r}) - 2jk_0Y_0 \iint_S \bar{\bar{G}}_0(\mathbf{r},\mathbf{r}') \bullet [\mathbf{E}(\mathbf{r}') \times \hat{\mathbf{z}}]\, dS' \tag{3}$$

where $\mathbf{H}^{inc}$ denotes the incident field due to possible external sources ($\mathbf{J}^{ext}$, $\mathbf{M}^{ext}$), $\mathbf{H}^{ref}$ is that reflected by the ground plane without the aperture, and $\bar{\bar{G}}_0$ is the usual free-space dyadic Green's function. Enforcing continuity of the tangential electric and magnetic fields across the aperture, we may substitute (3) into (2) to find

$$\begin{aligned} F(\mathbf{E}) \;=\; & \frac{1}{2}\iiint_V \left[\frac{1}{\mu_r}(\nabla \times \mathbf{E}) \bullet (\nabla \times \mathbf{E}) - k_0^2 \epsilon_r \mathbf{E} \bullet \mathbf{E}\right] dV \\ & + \iiint_V \left[jk_0 Z_0 \mathbf{J}^{int} \bullet \mathbf{E} - \frac{1}{\mu_r}\mathbf{M}^{int} \bullet (\nabla \times \mathbf{E})\right] dV \\ & -2k_0^2 \iint_S [\mathbf{E}(\mathbf{r}) \times \hat{\mathbf{z}}] \bullet \left[\iint_S \bar{\bar{G}}_0(\mathbf{r},\mathbf{r}') \bullet [\mathbf{E}(\mathbf{r}') \times \hat{\mathbf{z}}]\, dS'\right] dS \\ & -2jk_0 Z_0 \iint_S [\mathbf{E}(\mathbf{r}) \times \hat{\mathbf{z}}] \bullet \mathbf{H}^{inc}(\mathbf{r})\, dS \end{aligned} \tag{4}$$

which involves only the electric field and can be discretized in the usual context of the finite element method for a solution of the cavity and aperture fields.

To discretize (4), the volume V is subdivided into small volume elements such as tetrahedra, triangular prisms, or rectangular bricks. Accordingly, using the edge-based vector basis functions, the electric field $\mathbf{E}$ is expanded as

$$\mathbf{E} = \sum_{j=1}^{N} E_j \mathbf{W}_j \tag{5}$$

where N denotes the total number of element edges resulting from the subdivision, excluding those coinciding with conducting surfaces since the tangential components of

the electric field associated with those edges are zero. Also, E_j denote the unknown expansion coefficients equal to the element edge fields and $\mathbf{W}_j$ are the chosen vector basis functions. By substituting (5) into (4) and taking partial derivative of F with respect to E_i, we obtain

$$\begin{aligned}\frac{\partial F}{\partial E_i} &= \sum_{j=1}^{N} E_j \iiint_V \left[\frac{1}{\mu_r}(\nabla \times \mathbf{W}_i) \bullet (\nabla \times \mathbf{W}_j) - k_0^2 \epsilon_r \mathbf{W}_i \bullet \mathbf{W}_j\right] dV \\ &+ \iiint_V \left[jk_0 Z_0 \mathbf{J}^{int} \bullet \mathbf{W}_i - \frac{1}{\mu_r}\mathbf{M}^{int} \bullet (\nabla \times \mathbf{W}_i)\right] dV \\ &-2k_0^2 \chi_i \iint_S [\mathbf{W}_i \times \hat{\mathbf{z}}] \bullet \sum_{j=1}^{N} \chi_j E_j \left[\iint_S \bar{\bar{G}}_0 \bullet \left[\mathbf{W}_j' \times \hat{\mathbf{z}}\right] dS'\right] dS \\ &-2jk_0 Z_0 \chi_i \iint_S [\mathbf{W}_i \times \hat{\mathbf{z}}] \bullet \mathbf{H}^{inc}\, dS \end{aligned} \tag{6}$$

where $\chi_i = 1$ when the ith edge lies on the aperture S and $\chi_i = 0$ elsewhere. The final system of equations is then obtained by imposing the stationarity condition (1), i.e., by letting $\partial F/\partial E_i = 0$ for $i = 1, 2, ..., N$.

It remains to choose the vector basis functions $\mathbf{W}_j$ and this depends on the choice of volume elements. However, if rectangular bricks are chosen for the discretization, the surface integral can be cast in the form of the discrete Fourier transform. As a result the FFT can be used for its evaluation when an iterative solution such as the conjugate or biconjugate gradient method is employed. This circumvents a need to generate and store the full submatrix, thus retaining the $O(N)$ storage requirement for solving the system.

The modelling of the conducting patches, microstrip transmission lines, impedance loads, shorting pins and coaxial feeds can be considered in the context of the finite element formulation. Specifically, the radiating patches and transmission lines are modelled by setting the tangential electric field components to zero on a conducting surface; the impedance load (or conducting pin) is modelled as a post of finite (or infinite) conduc-

tivity joining both the patch and the base of the cavity. Finally, the coaxial feed can be modelled either by an electric current filament or by a magnetic frill current. The input impedance can be simply calculated as the voltage observed at the feed point for a unit electric current input.

III. EXPERIMENTAL SETUP

To experimentally verify the proposed formulation for scattering computations, a low cross section body was designed and built to serve as the test platform. This test body is shown in Figure 2 and its top surface is intended to simulate the infinite ground plane and is diamond shaped to minimize its scattering when there is no patch or cavity aperture on its surface. The bottom of the test body was designed to house the test antenna with minimal interference to the aperture scattering. A removable diamond-shaped plate was placed on the top flat surface of the test body to permit the mounting of different test antenna structures or other targets. The test body was first measured by itself in the University of Michigan tapered anechoic chamber as shown in Figure 3. Without the presence of a cavity (i.e., the removable plate was plat and uncut), the radar cross section of the test body by itself was measured to be less than -45 dBsm in the principal plane for incidences to 10 degrees from the broadside. Additional reduction to the RCS level of the test body could have been achieved with some treatment but this was not deemed necessary at this time. Further, it should be pointed out that because of the finiteness of the test body, the infinite ground plane simulation is comprised near grazing. In particular, it will be seen that the measured data should be representative of the ground plane simulation for incidences above 10 degrees from grazing.

IV. NUMERICAL AND EXPERIMENTAL RESULTS

A. Experimental Verification

The specific patch geometry which was measured was a 1.448 in. × 1.083 in. rectangular patch residing on a dielectric substrate having thickness $t = 0.057$ in. and relative permittivity $\epsilon_r \approx 4.0$. The substrate was housed in a 2.89 in. × 2.10 in. × 0.057 in. rectangular cavity recessed in a ground plane. The incident plane wave was polarized along the $\hat{\theta}$ direction and the backscatter radar cross section (RCS) was measured as a function of the angle of incidence in the plane perpendicular to the patch and parallel to its longer dimension.

Figures 4-7 show the backscatter RCS at four different frequencies (9.2 GHz, 9.64 GHz, 10.0 GHz and 10.8 GHz) of the filled cavity stucture with the patch removed. Figures 8-11 show the backscatter RCS at the same four frequencies with the patch now placed on the surface of the substrate. Good agreement is observed between measurements and calculations in all cases for the incidence angles within the range of 10-80 degrees. As noted above, the measured data near grazing angles and near broadside are in error because of contributions from the low cross section body.

B. Input Impedance Calculations

To validate the computation of the input impedance via the hybrid finite element method we compare the calculated input impedance of a microstrip antenna excited by a filament of uniform current to corresponding results based on the moment method solution [5] and data measured for a coaxially fed microstrip antenna. We note that whereas the measured data and moment method solution [5] were based on the infinite substrate model our computations were made for the patch antenna on the substrate which fills a 5.1 cm × 7.5 cm × 0.08779 cm cavity recessed in a ground plane. Experi-

mental calculations showed, however, that in this case the effect of the cavity termination on the input impedance is negligible. Figure 12 shows the input impedance locus near the first resonance whereas Figure 13 displays similar results in the vicinity of the second resonance, both plotted on a Smith Chart. It is observed that the results based on this method are in good agreement with the moment method solution and the measured data except for a slight frequency shift of 1%. Figures 14 and 15 show the input impedance for a loaded microstrip antenna and in this case it is seen that our calculations are in better agreement with the measurements. To further demonstrate the capability of the method, Figures 16 and 17 show the calculated input impedance for an unloaded and shorted microstrip antenna.

CONCLUSIONS

s report, we presented experimental verification of the scattering and input impedance computations for patch antennas obtained via the hybrid finite element - boundary integral method. The RCS measurements were obtained by placing the patch antenna in a cavity which was housed in a low cross section body. Scattering patterns were measured for single unloaded patches and the measured data were compared with the computed results. Good agreement was observed between the measurements and calculations in all cases. The input impedance computations were compared with measured data available in the literature. Again, good agreement agreement was observed in spite of the approximate input terminal model (probe) employed for those calculations.

ACKNOWLEGEMENTS

The authors wish to thank Dr. V. V. Liepa and Mr. Changyul Cheon for performing the measurements.

REFERENCES

[1] J. M. Jin and J. L. Volakis, "A finite element – boundary integral formulation for scattering by three-dimensional cavity-backed apertures," *IEEE Trans. Antennas Propagat.*, vol. AP-39, pp. 97-104, Jan. 1991.

[2] J. M. Jin and J. L. Volakis, "Electromagnetic scattering by and transmission through a three-dimensional slot in a thick conducting plane," *IEEE Trans. Antennas Propagat.*, vol. AP-39, pp. 543-550, April 1991.

[3] J. M. Jin and J. L. Volakis, "Electromagnetic scattering and radiation from microstrip patch antennas and arrays residing in a cavity," Univ. of Michigan Radiation Lab. Report 027723-1-T, Aug. 1990.

[4] J. M. Jin and J. L. Volakis, "Scattering and radiation from microstrip patch antennas and arrays residing in a cavity," Univ. of Michigan Radiation Lab. Report 027723-2-T, Jan. 1991.

[5] D. P. Forrai and E. H. Newman, "Radiation and scattering from loaded microstrip antennas over a wide bandwidth," Ohio State University Technical Report No. 719493-1, Sept. 1988.

FIGURE CAPTIONS

Fig. 1 Geometry of a microstrip patch array in a cavity.

Fig. 2 The low cross section test body serving as the test platform.

Fig. 3 Experimental setup.

Fig. 4 A comparison of the computed (dots) and measured (solid line) θ-polarized RCS of a rectangular cavity recessed in a ground plane at 9.2 GHz.

Fig. 5 A comparison of the computed (dots) and measured (solid line) θ-polarized RCS of a rectangular cavity recessed in a ground plane at 9.64 GHz.

Fig. 6 A comparison of the computed (dots) and measured (solid line) θ-polarized RCS of a rectangular cavity recessed in a ground plane at 10 GHz.

Fig. 7 A comparison of the computed (dots) and measured (solid line) θ-polarized RCS of a rectangular cavity recessed in a ground plane at 10.8 GHz.

Fig. 8 A comparison of the computed (dots) and measured (solid line) θ-polarized RCS of a rectangular patch on a substrate filling a rectangular cavity recessed in a ground plane at 9.2 GHz.

Fig. 9 A comparison of the computed (dots) and measured (solid line) θ-polarized RCS of a rectangular patch on a substrate filling a rectangular cavity recessed in a ground plane at 9.64 GHz.

Fig. 10 A comparison of the computed (dots) and measured (solid line) θ-polarized RCS of a rectangular patch on a substrate filling a rectangular cavity recessed in a ground plane at 10 GHz.

Fig. 11 A comparison of the computed (dots) and measured (solid line) θ-polarized RCS of a rectangular patch on a substrate filling a rectangular cavity recessed in a ground plane at 10.8 GHz.

Fig. 12 A comparison of the computed and measured input impedance near and at the first resonance for a microstrip patch antenna.

Fig. 13 A comparison of the computed and measured input impedance near and at the second resonance for a microstrip patch antenna.

Fig. 14 A comparison of the computed and measured real part of the input impedance for a loaded microstrip patch antenna.

Fig. 15 A comparison of the computed and measured reactive part of the input impedance for a loaded microstrip patch antenna.

Fig. 16 A comparison of the computed real part of the input impedance for an unloaded and shorted microstrip patch antenna.

Fig. 17 A comparison of the computed reactive part of the input impedance for an unloaded and shorted microstrip patch antenna.

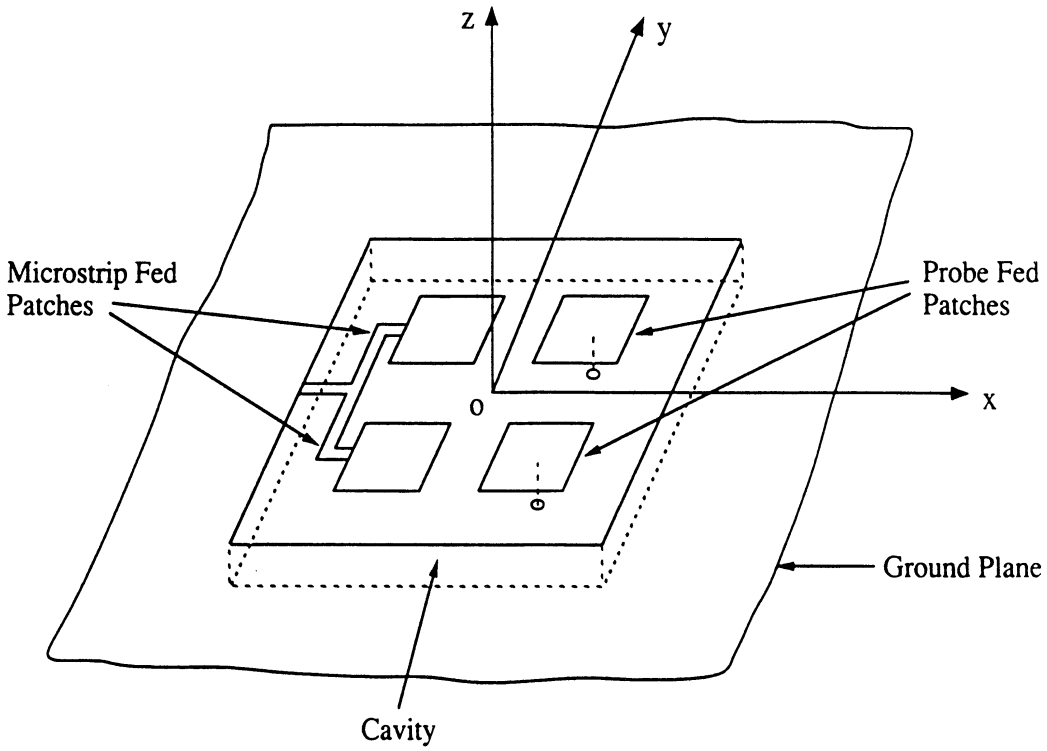

Fig. 1 Geometry of a microstrip patch array in a cavity.

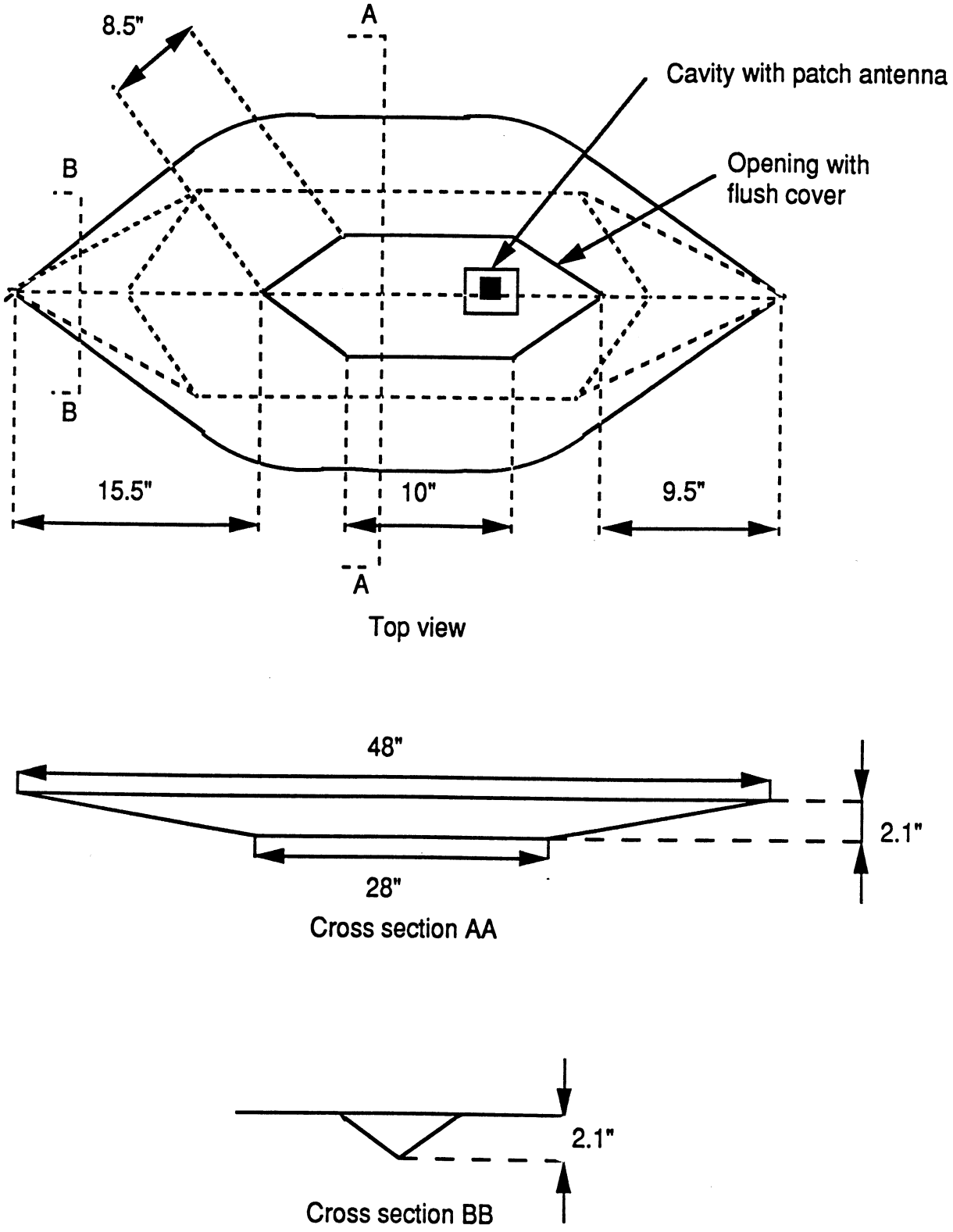

Fig. 2 The low cross section test body serving as the test platform.

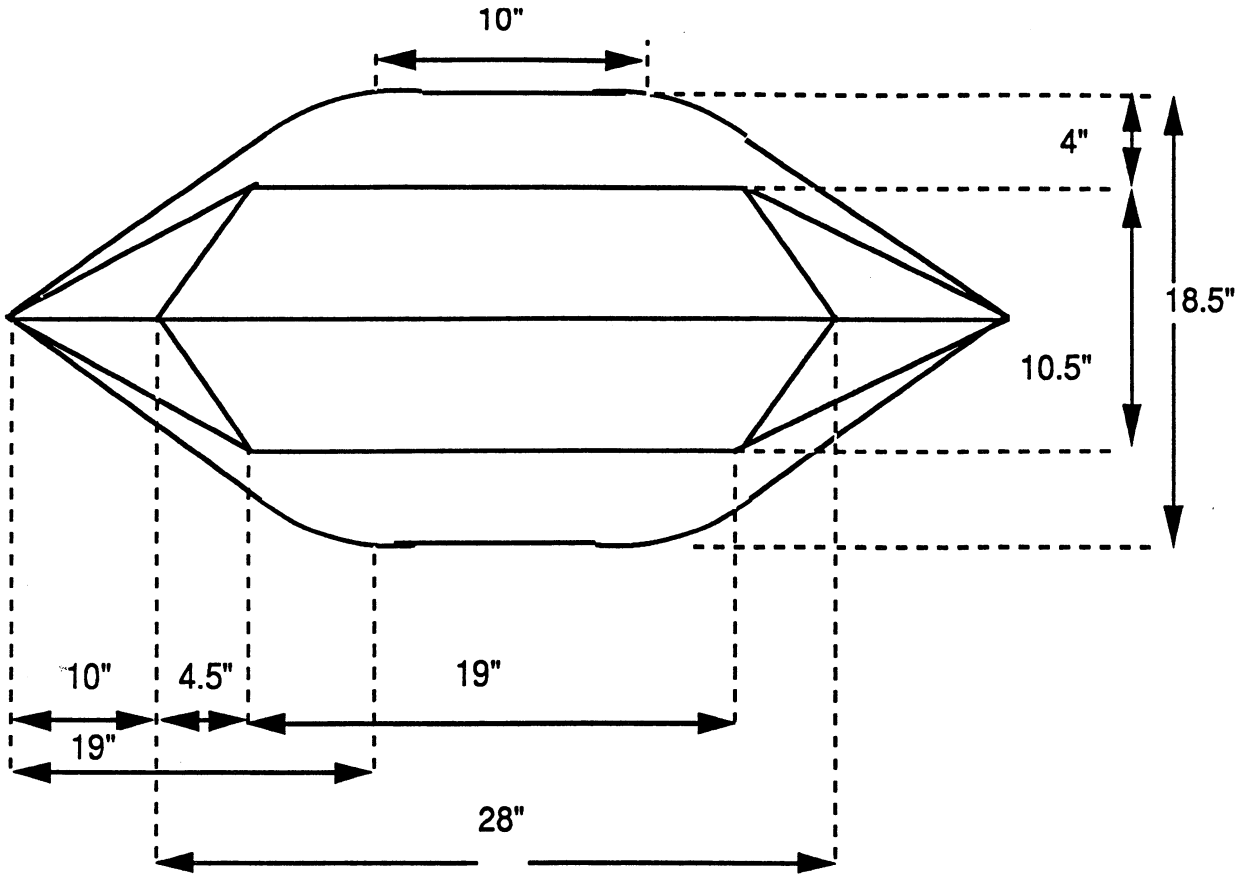

Bottom View

Fig. 2 The low cross section test body serving as the test platform (Cont'd).

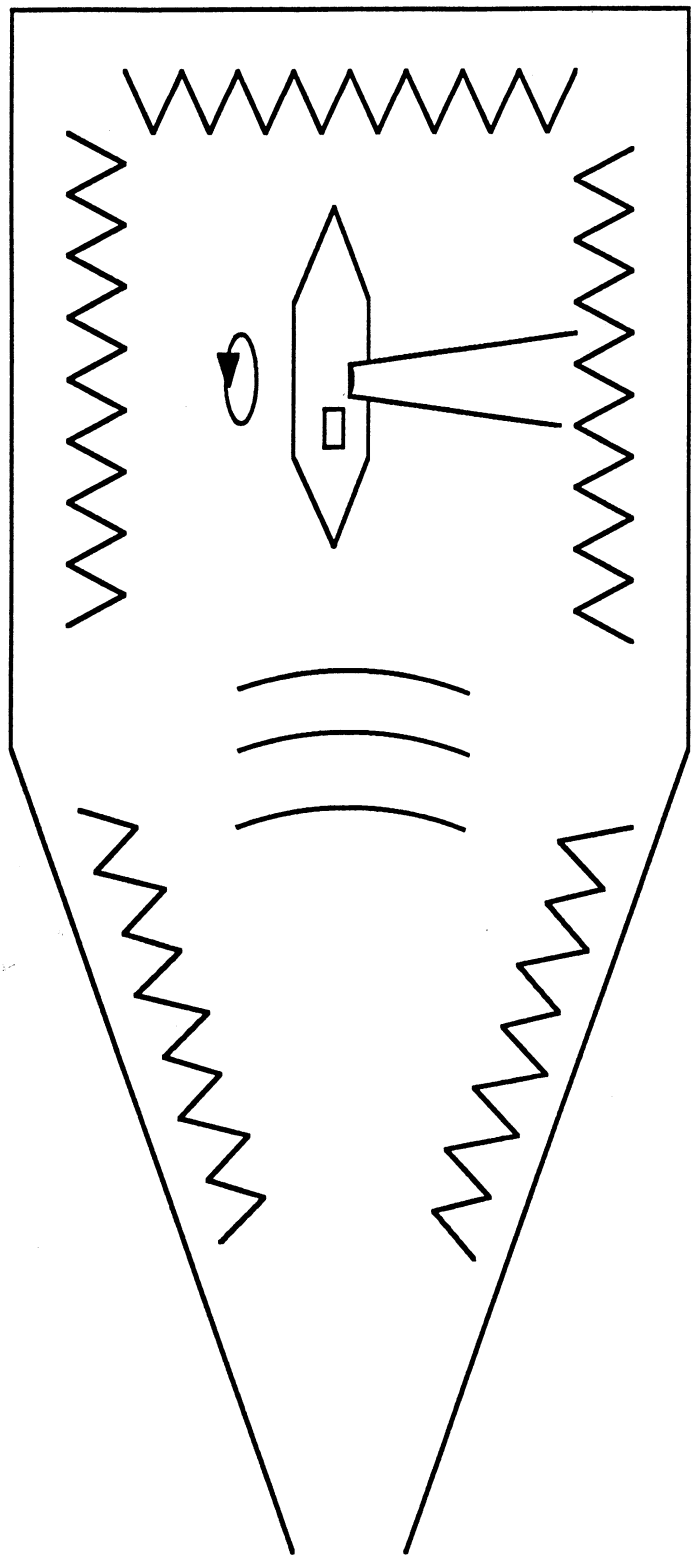

Fig. 3 Experimental setup.

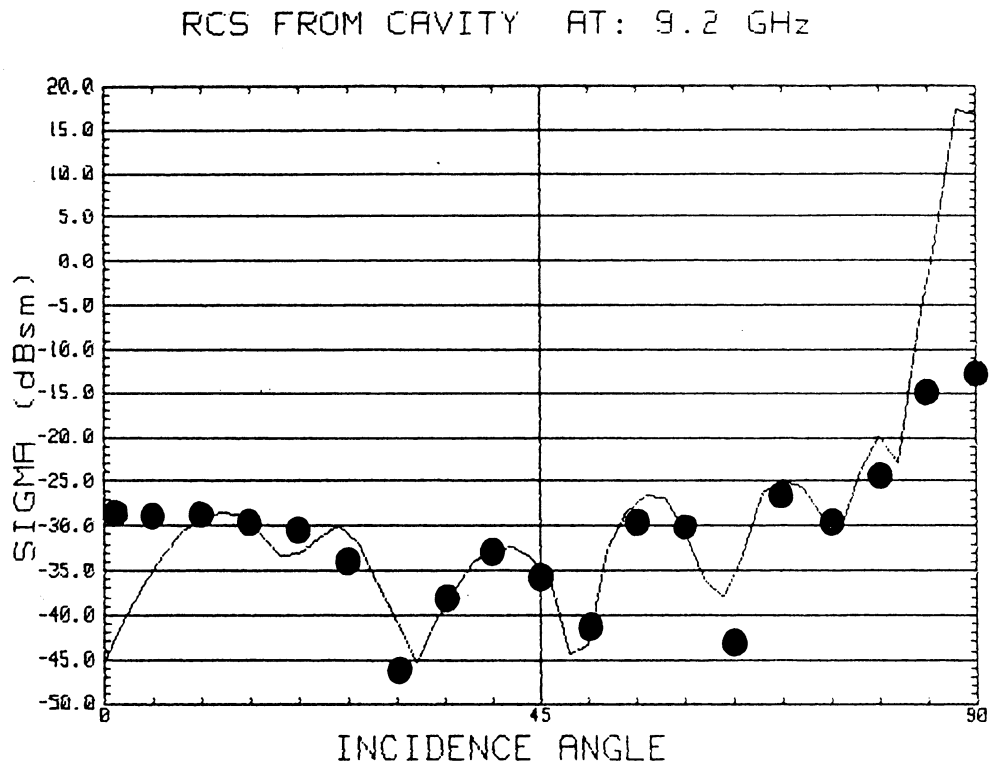

Fig. 4 A comparison of the computed (dots) and measured (solid line) θ-polarized RCS of a rectangular cavity recessed in a ground plane at 9.2 GHz.

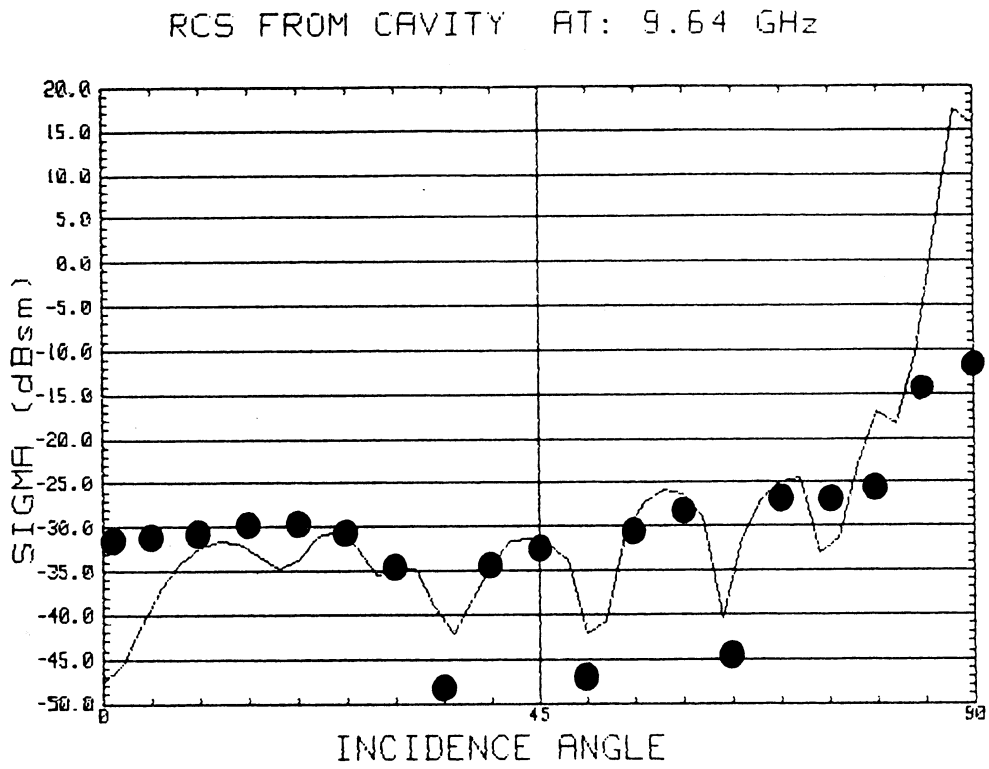

Fig. 5 A comparison of the computed (dots) and measured (solid line) θ-polarized RCS of a rectangular cavity recessed in a ground plane at 9.64 GHz.

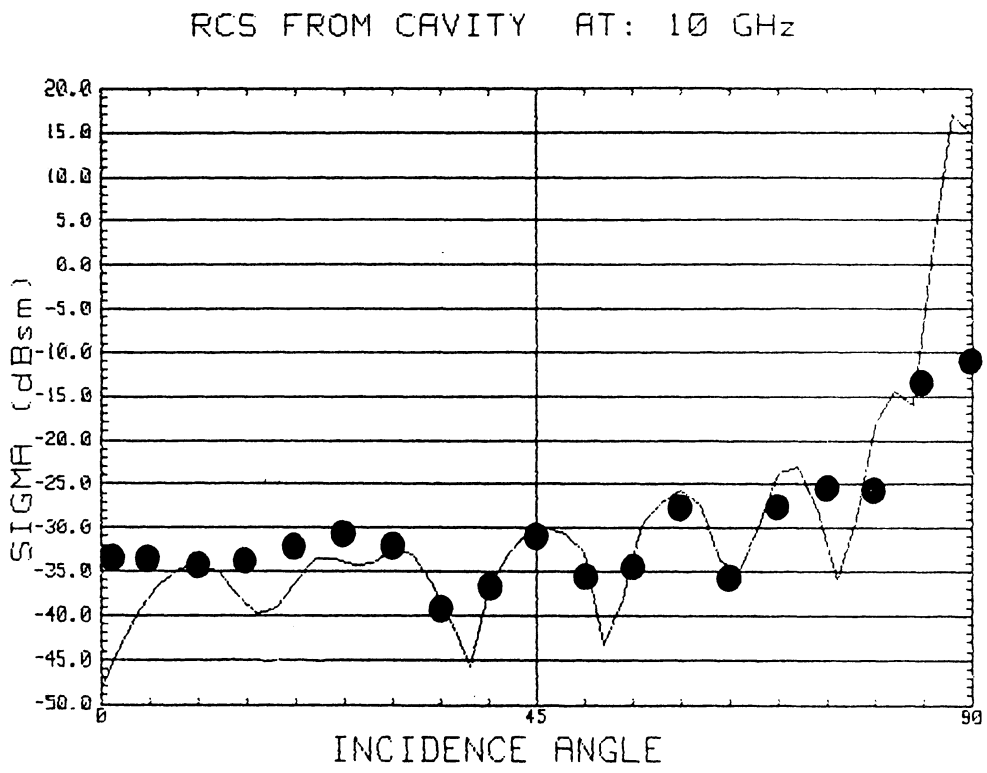

Fig. 6 A comparison of the computed (dots) and measured (solid line) θ-polarized RCS of a rectangular cavity recessed in a ground plane at 10 GHz.

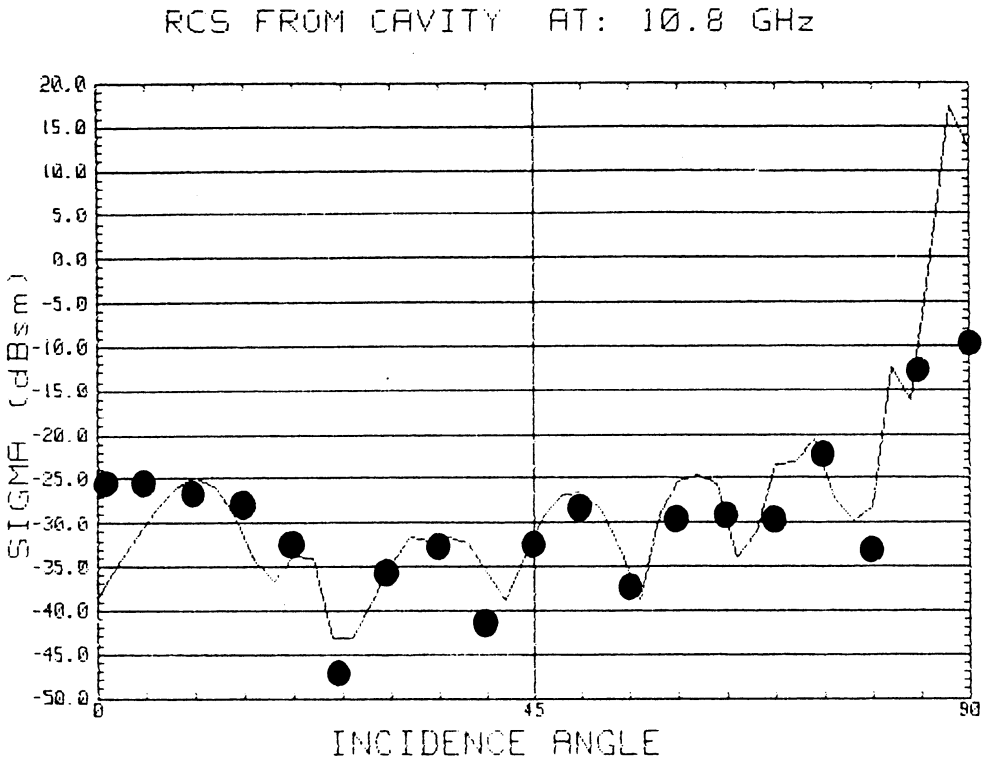

Fig. 7 A comparison of the computed (dots) and measured (solid line) θ-polarized RCS of a rectangular cavity recessed in a ground plane at 10.8 GHz.

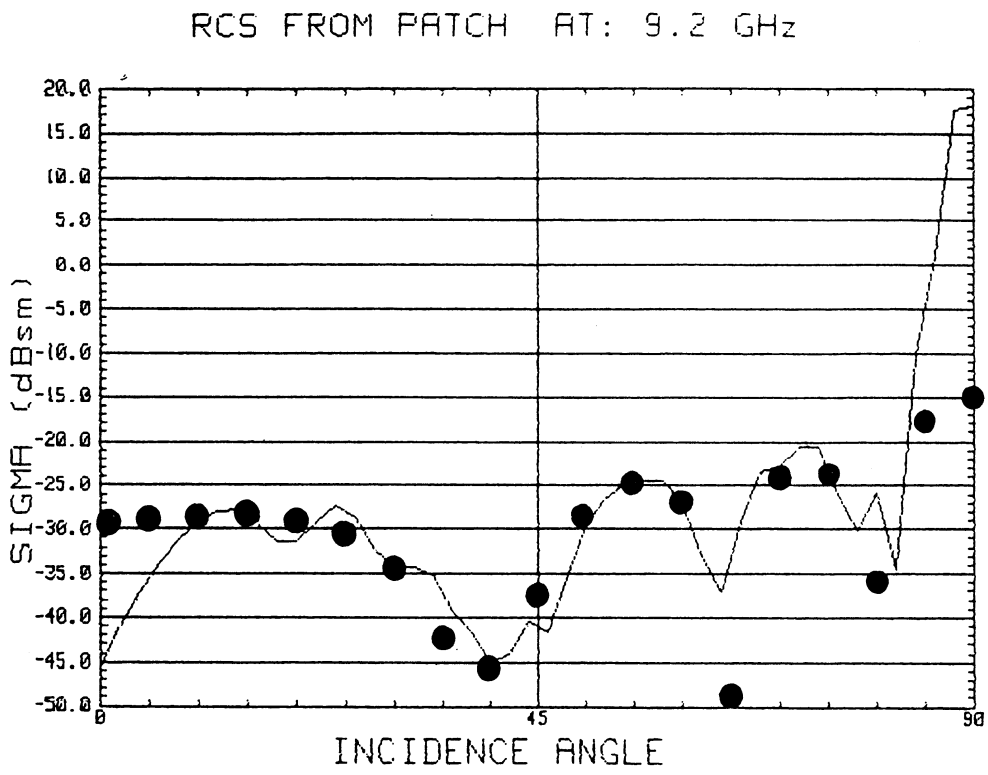

Fig. 8 A comparison of the computed (dots) and measured (solid line) θ-polarized RCS of a rectangular patch on a substrate filling a rectangular cavity recessed in a ground plane at 9.2 GHz.

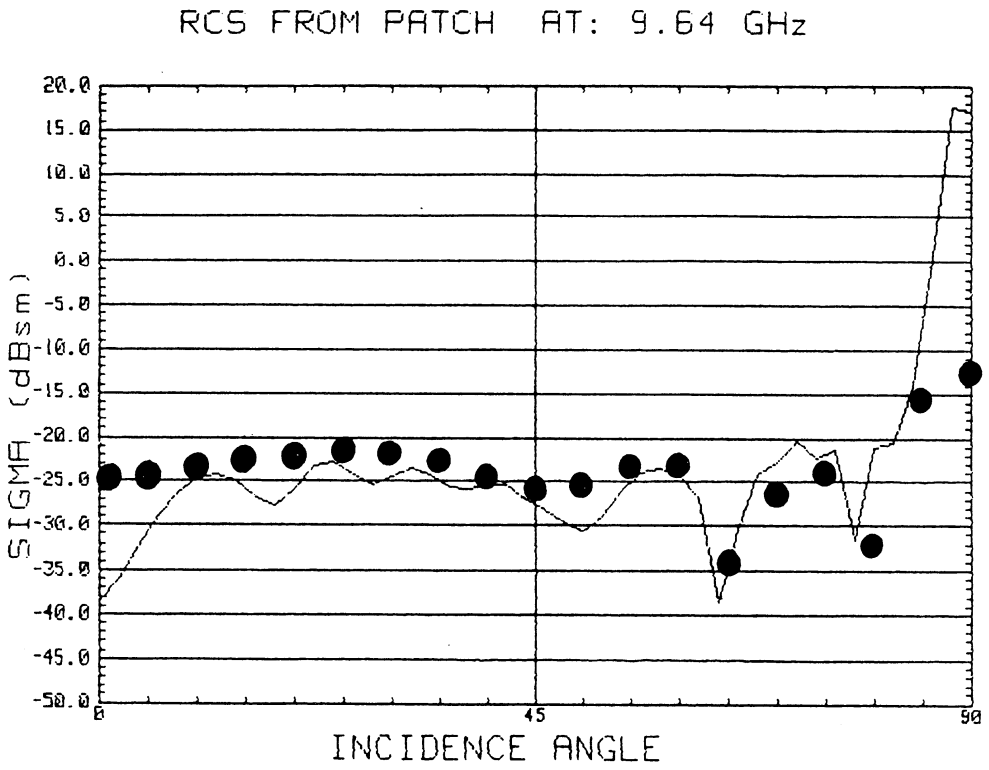

Fig. 9 A comparison of the computed (dots) and measured (solid line) θ-polarized RCS of a rectangular patch on a substrate filling a rectangular cavity recessed in a ground plane at 9.64 GHz.

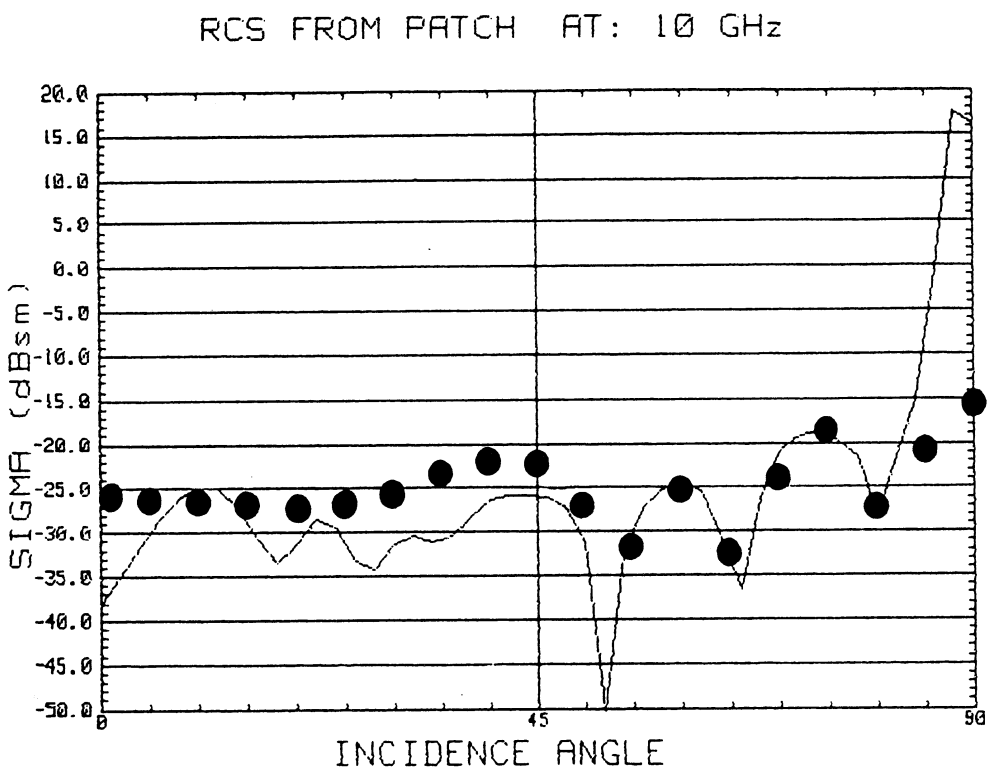

Fig. 10 A comparison of the computed (dots) and measured (solid line) θ-polarized RCS of a rectangular patch on a substrate filling a rectangular cavity recessed in a ground plane at 10 GHz.

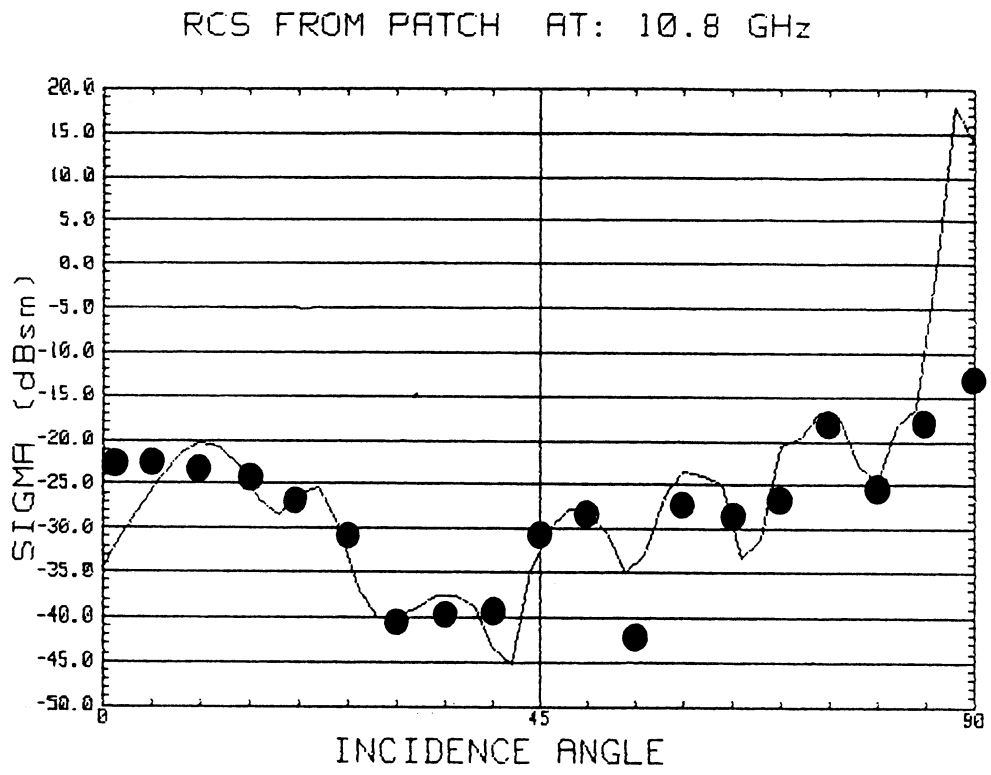

Fig. 11 A comparison of the computed (dots) and measured (solid line) θ-polarized RCS of a rectangular patch on a substrate filling a rectangular cavity recessed in a ground plane at 10.8 GHz.

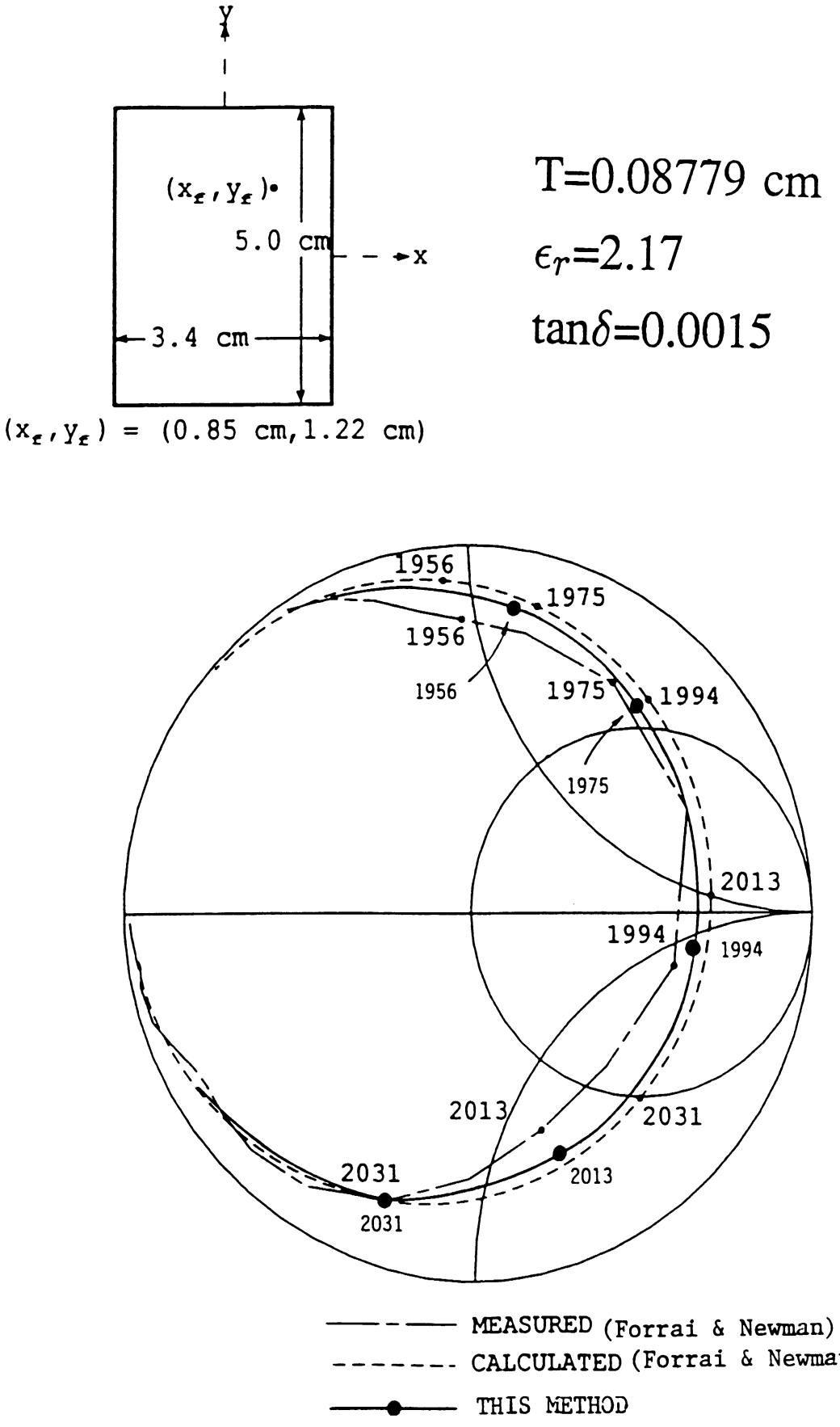

Fig. 12 A comparison of the computed and measured input impedance near and at the first resonance for a microstrip patch antenna.

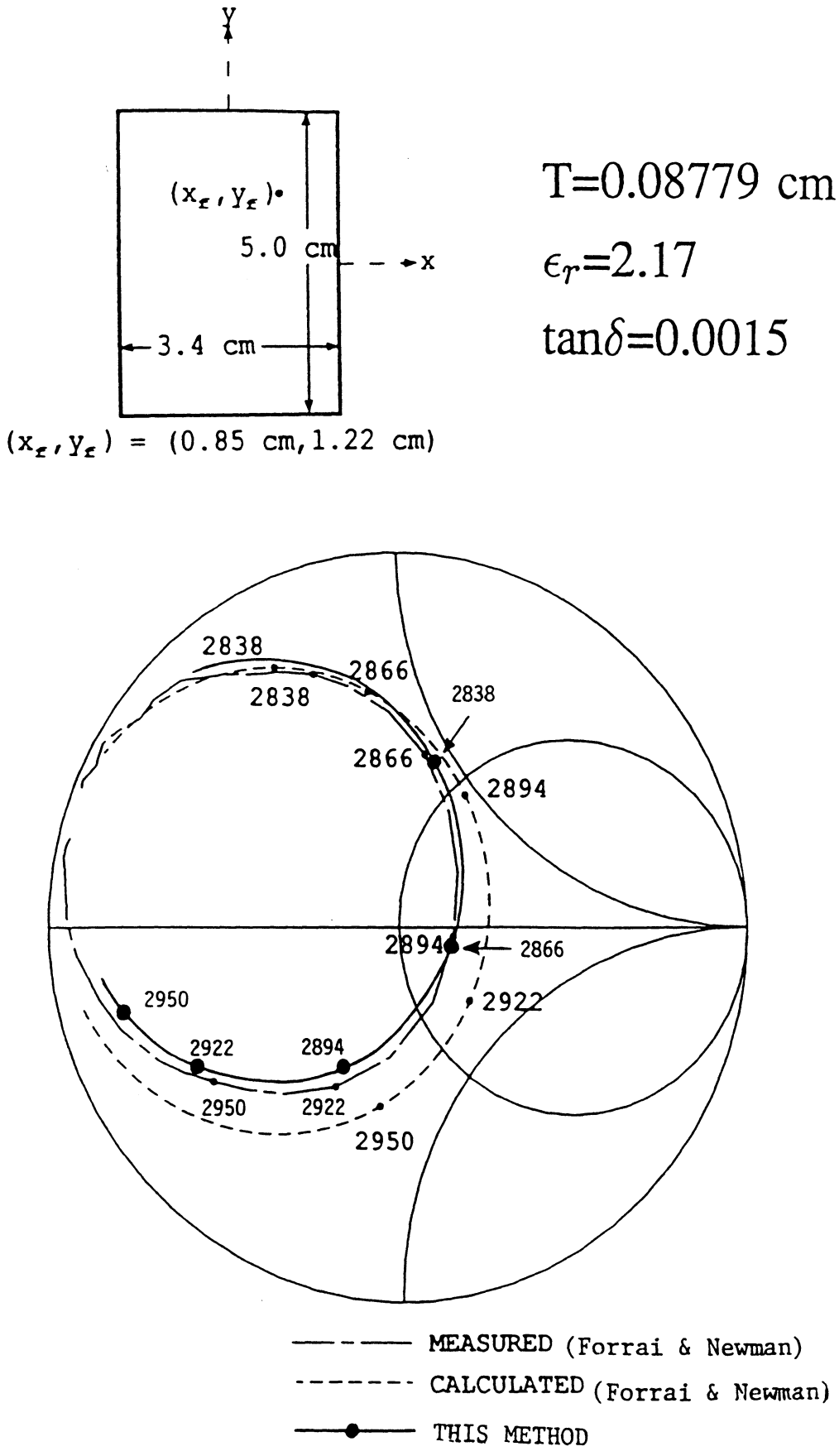

Fig. 13 A comparison of the computed and measured input impedance near and at the second resonance for a microstrip patch antenna.

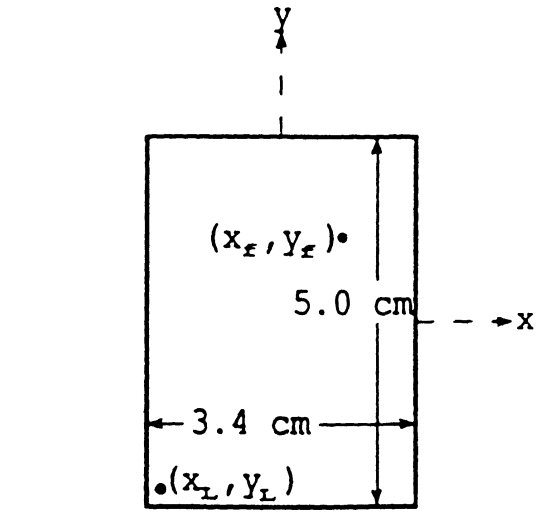

(x_f, y_f) = (0.85 cm, 1.22 cm)
(x_L, y_L) = (-1.5 cm, -2.2 cm)

T=0.08779 cm

ϵ_r=2.17

tanδ=0.0015

Z_L = 50 ohms

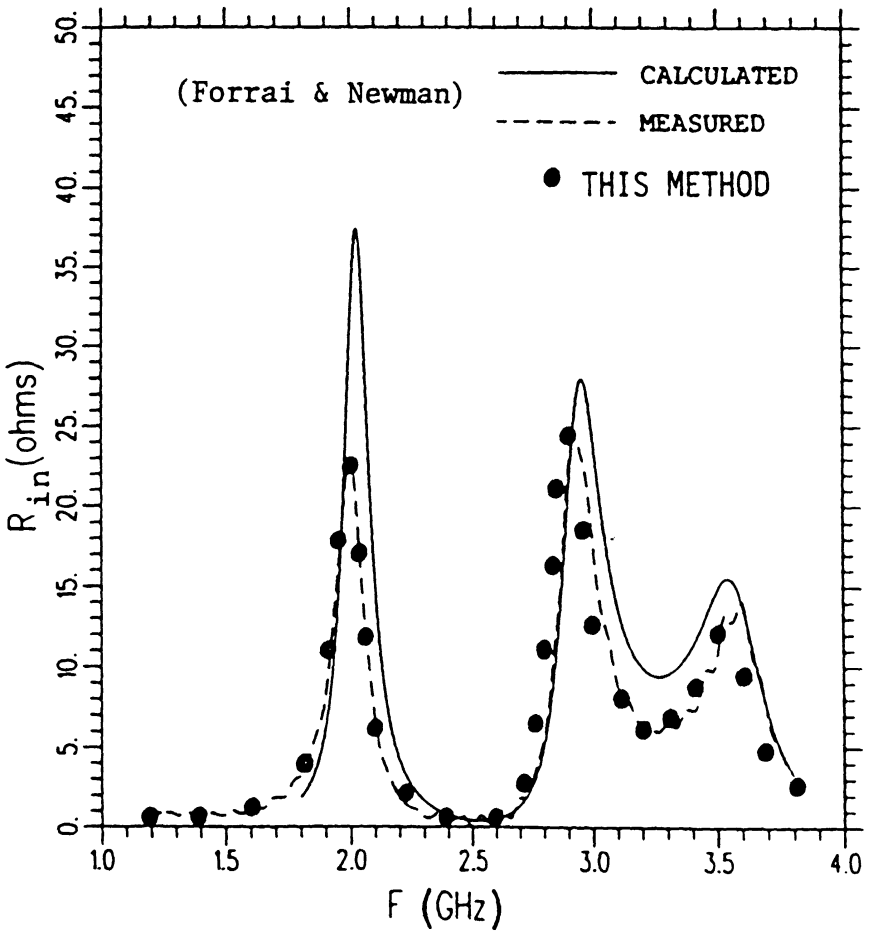

Fig. 14 A comparison of the computed and measured real part of the input impedance for a loaded microstrip patch antenna.

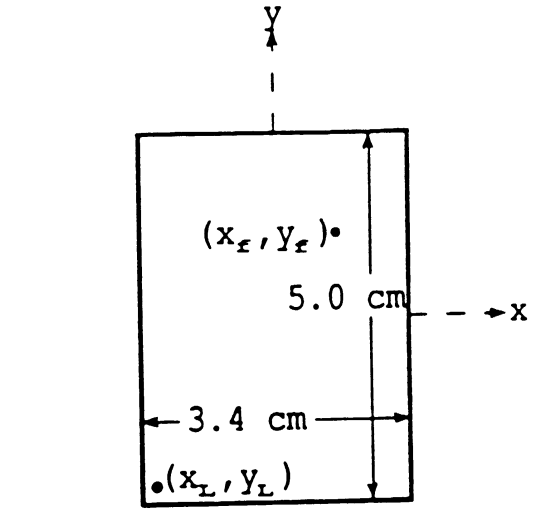

(x_f, y_f) = (0.85 cm, 1.22 cm)
(x_L, y_L) = (-1.5 cm, -2.2 cm)

T=0.08779 cm

ϵ_r=2.17

tanδ=0.0015

Z_L = 50 ohms

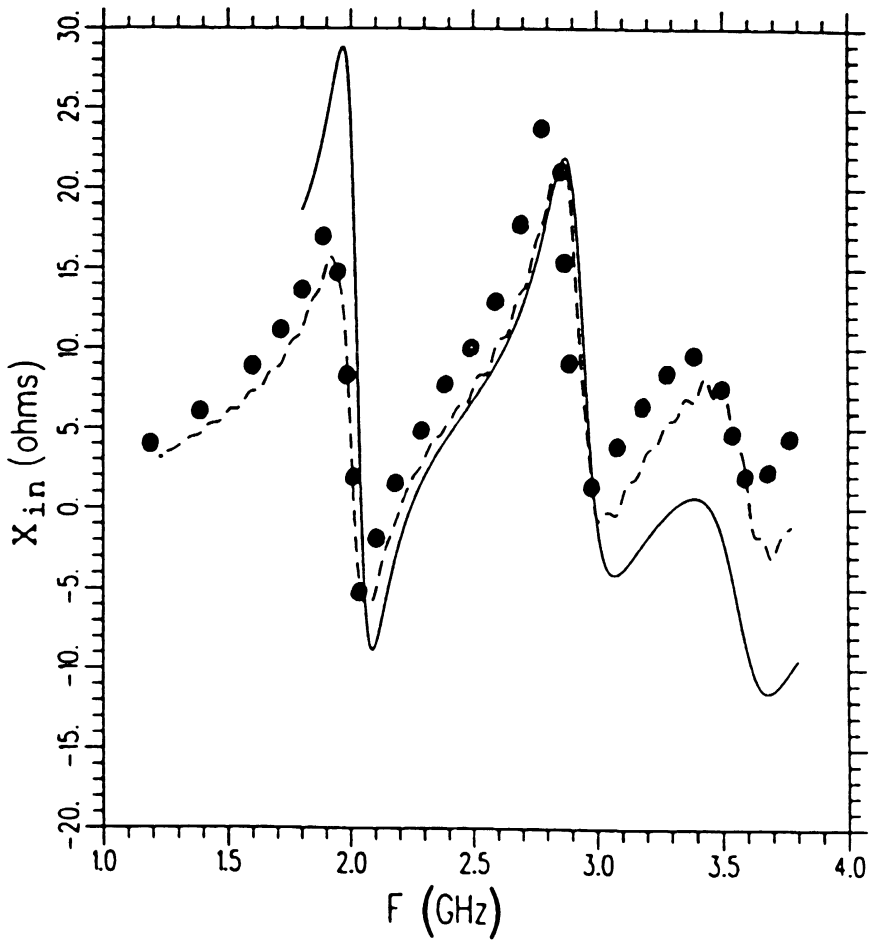

Fig. 15 A comparison of the computed and measured reactive part of the input impedance for a loaded microstrip patch antenna.

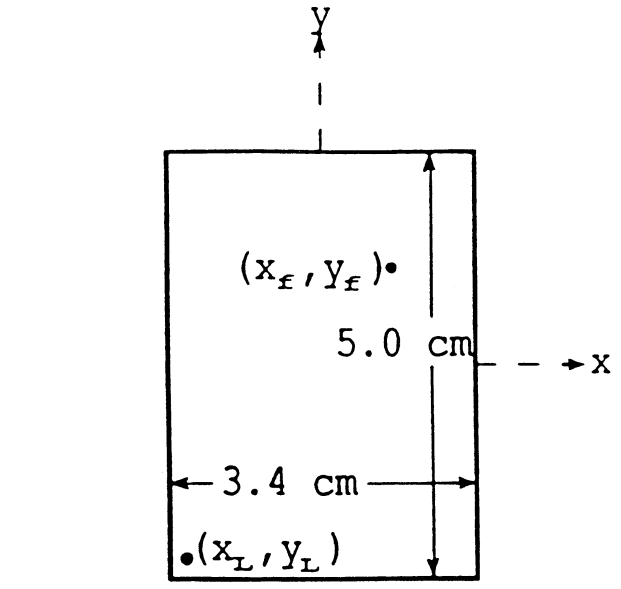

(x_f, y_f) = (0.85 cm, 1.22 cm)
(x_L, y_L) = (-1.5 cm, -2.2 cm)

T=0.08779 cm

ϵ_r=2.17

tanδ=0.0015

Z_L = 0 ohms

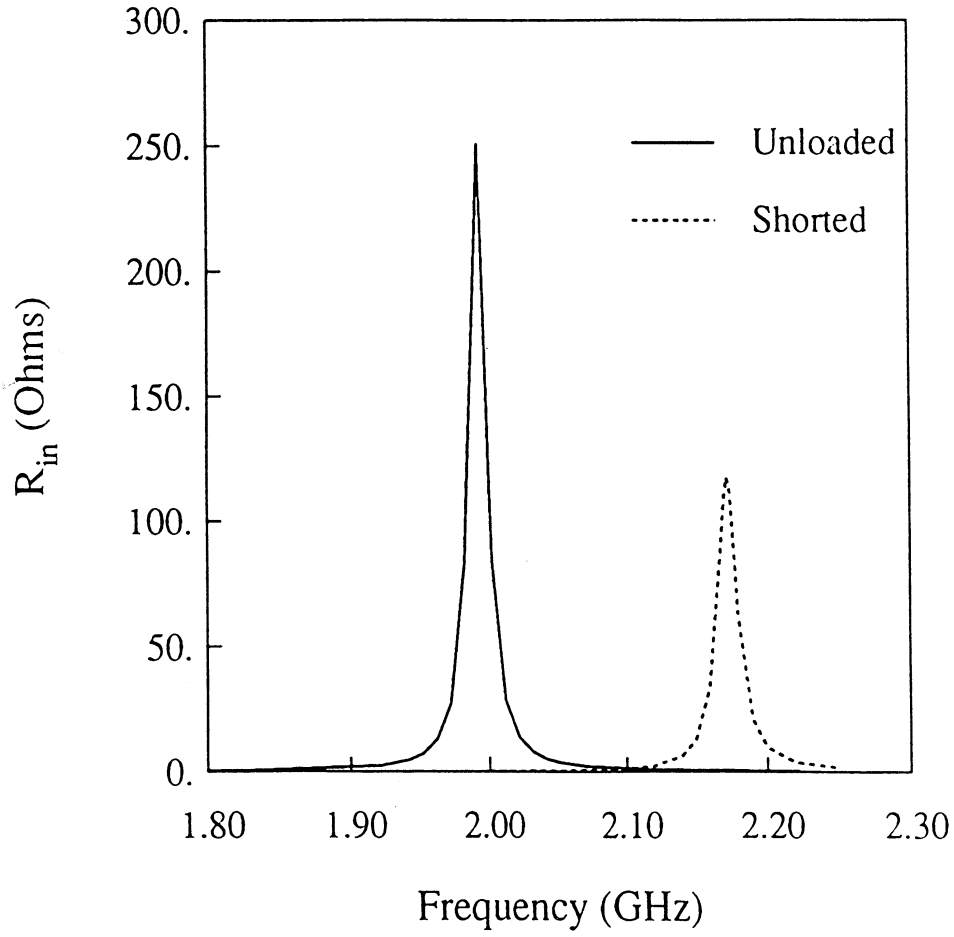

Fig. 16 A comparison of the computed real part of the input impedance for an unloaded and shorted microstrip patch antenna.

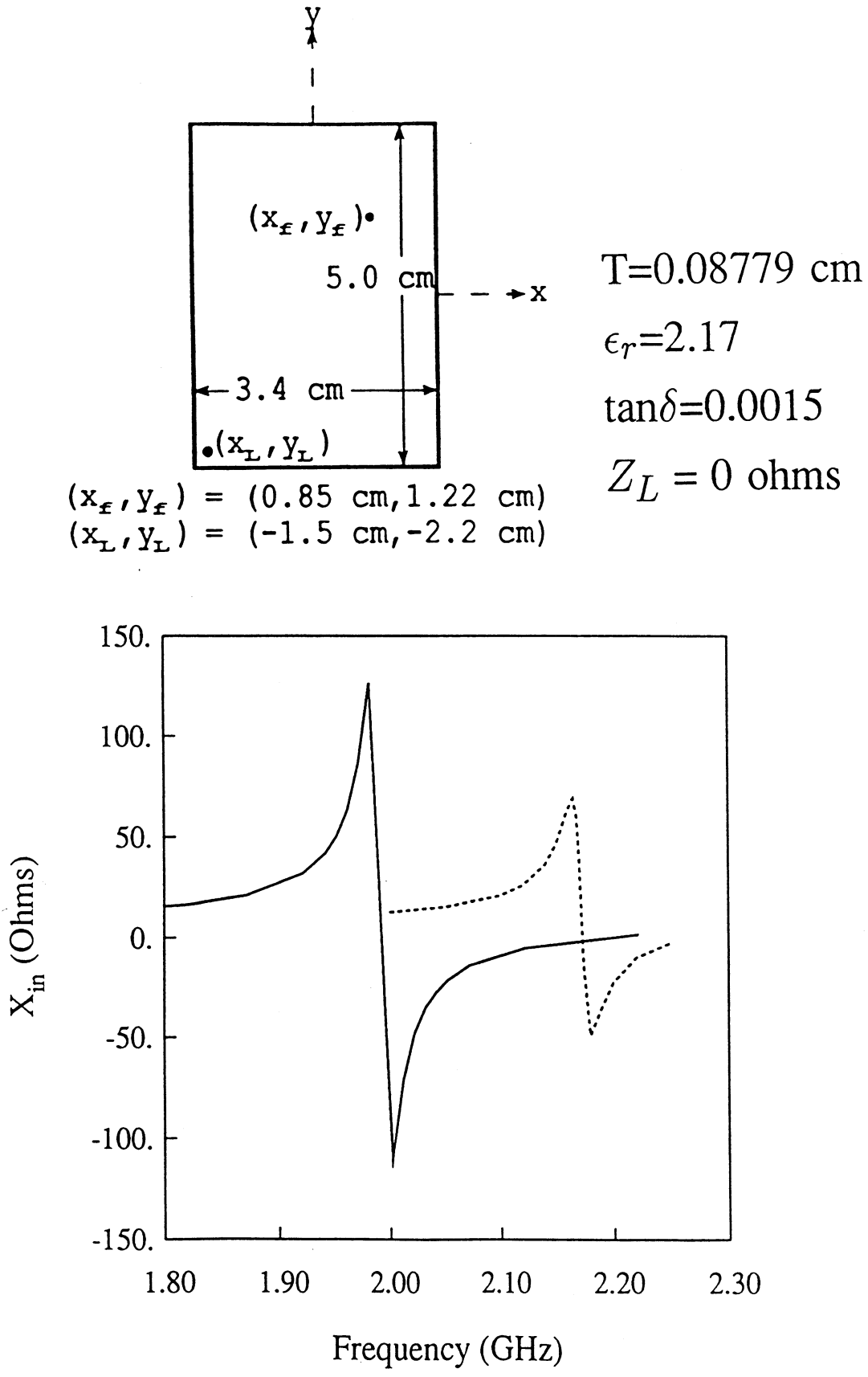

Fig. 17 A comparison of the computed reactive part of the input impedance for an unloaded and shorted microstrip patch antenna.

Modeling of Resistive Sheets in Finite Element Solutions

J.M. Jin, J.L. Volakis
Radiation Laboratory
Department of Electrical Engineering and Computer Science
University of Michigan
Ann Arbor, MI 48109-2122

C.L. Yu
Pacific Missile Test Center
Pt. Mugu, CA 93042-5000
and
A.C. Woo
NASA-Ames Research Center
Moffett Field, CA 94035-1000

Abstract

A formulation is presented for modeling resistive sheet in the context of the finite element method. The appropriate variational function is derived and results are presented for scattering by resistively loaded metal-backed cavity which are used to validate the formulation.

1 Introduction

A resistive card is an infinitesimally thin sheet of material which allows partial penetration of the electromagnetic field. Thin dielectric layers and very thin conductors whose thickness is less than the skin depth are examples of materials which can be modelled by resistive cards or sheets. Resistive cards are often used for radar cross section and RF power penetration control and as a result they have been studied extensively. Such studies have generally been done in the context of high frequency [1,2] and integral equation solutions [3,4], but to date the treatment of resistive cards within the context of the finite element method (FEM) has not been considered. Over the past few years, FEM has been applied to a variety of electromagnetic applications and it is thus important to incorporate the modeling of resistive cards in the FEM. In this paper we propose an FEM formulation which accounts for the presence of resistive sheets. To validate this formulation results based on a physical modeling of the resistive sheet are also presented. In this case, the resistive sheet is equivalently replaced by a thin dielectric layer. The modeling of such a layer in the usual manner leads to larger and consequently inefficient linear systems, which is the primary reason for resorting to a mathematical modeling of the resistive sheet. Results based on the mathematical and physical modeling of the resistive sheet are presented in connection with the scattering by a metal-backed cavity in a ground plane. These are used to validate the proposed mathematical model of the resistive sheet in the context of the FEM.

2 Formulation

A resistive sheet is characterized by its resistivity R which is measured in Ohms per square. Mathematically, it satisfies the boundary condition [4]

$$\hat{n} \times (\hat{n} \times \mathbf{E}) = -R\hat{n} \times \left(\mathbf{H}^{+} - \mathbf{H}^{-}\right) \tag{1}$$

where $\mathbf{H}^{\pm}$ denotes the magnetic field above and below the sheet, $\mathbf{E}$ is the electric field and its tangential component is continuous across the sheet, and $\hat{n}$ denotes the unit normal to the sheet pointing in the upward direction (+ side). To a first order, this boundary condition can be used to simulate

the presence of a thin dielectric layer of material by setting [5]

$$R = \frac{Z_o}{jk_o(\epsilon_r - 1)t}$$

In this, t is the thickness of the layer, Z_o and k_o denote the free space intrinsic impedance and wave number, respectively, and ϵ_r is the relative dielectric constant of the layer. Alternatively, a resistive sheet may be equivalently replaced by a thin dielectric layer having thickness t and a relative permittivity of

$$\epsilon_r = 1 - \frac{jZ_o}{k_o t R} \tag{2}$$

Generally, the accuracy of this simulation increases as the thickness t is decreased. Typically, t should not exceed 1/10th of the wavelength in the material.

Let us now consider a finite element solution of the fields within a volume V subject to a given excitation. The volume consists of some inhomogeneous dielectric having relative permittivity and permeability ϵ_r and μ_r, respectively, and we shall also assume that resistive cards may be embedded within the dielectric (see Figure 1). In accordance with the finite element method, the volume is subdivided into M smaller volume elements and in this case we require that the resistive cards are tangential to the boundary surface of these elements. A weak solution of the fields within the volume can be obtained by extremizing the functional

$$F = \sum_{e=1}^{M} F^e, \tag{3}$$

$$\begin{aligned} F^e &= \int\int\int_{V_e} \left[\frac{1}{\mu_r} (\nabla \times \mathbf{E}) \cdot (\nabla \times \mathbf{E}) - k_o^2 \epsilon_r \mathbf{E} \cdot \mathbf{E} \right] dv \\ &\quad + jk_o Z_o \oiint_{S_e} \mathbf{E} \cdot (\mathbf{H} \times \hat{n}_e)\, ds \end{aligned} \tag{4}$$

with respect to the electric field $\mathbf{E}$ including that implied in $\mathbf{H}$. In this expression, V_e is the volume of the element which is enclosed by the surface S_e and $\hat{n}_e$ denotes the outward normal to S_e.

Generally, for a dielectric volume not enclosing resistive sheets or other current sheets, the contributions of the surface integrals in (3)-(4) vanish everywhere except when S_e coincides with the outer surface S_o of the volume V. This is a consequence of field continuity across the elements, but if a portion of the element's surface coincides with a resistive sheet, then the surface integral in (4) does not vanish since the magnetic field is discontinuous as described in (1). Let us for example consider the surface S_{re} which borders the eth and $(e+1)$th elements, and is coincident with a resistive sheet of resistivity R. Then the contribution from this surface to the surface integral in (4) is

$$jk_oZ_o \int\int_{S_{re}} \mathbf{E} \cdot \left(\mathbf{H}^- \times \hat{n}_{re}\right) ds$$

from the eth element and

$$-jk_oZ_o \int\int_{S_{re}} \mathbf{E} \cdot \left(\mathbf{H}^+ \times \hat{n}_{re}\right) ds$$

from the $(e+1)$th element with $\hat{n}_{re}$ pointing from the eth to the $(e+1)$th element. Combining these two integrals, it follows that the contribution of the surface S_{re} to the surface integral in (4) is

$$\begin{aligned} & - jk_oZ_o \int\int_{S_{re}} \left[\mathbf{E} \cdot \left(\mathbf{H}^+ - \mathbf{H}^-\right) \times \hat{n}_{re}\right] ds \\ & = jk_oZ_o \int\int_{S_{re}} \frac{1}{R} \mathbf{E} \cdot \left[\hat{n}_{re} \times (\hat{n}_{re} \times \mathbf{E})\right] ds \\ & = jk_oZ_o \int\int_{S_{re}} \frac{1}{R} (\hat{n}_{re} \times \mathbf{E}) \cdot (\hat{n}_{re} \times \mathbf{E}) \, ds \end{aligned} \tag{5}$$

Consequently, the functional F may be rewritten as

$$\begin{aligned} F = & \sum_{e=1}^{M} \int\int\int_{V_e} \left\{ \frac{1}{\mu_r} (\nabla \times \mathbf{E}) \cdot (\nabla \times \mathbf{E}) - k_o^2 \epsilon_r \mathbf{E} \cdot \mathbf{E} \right\} dv \\ & + jk_oZ_o \int\int_{S_r} \frac{1}{R} (\hat{n}_r \times \mathbf{E}) \cdot (\hat{n}_r \times \mathbf{E}) \, ds \\ & + jk_oZ_o \oiint_{S_o} \mathbf{E} \cdot (\mathbf{H} \times \hat{n}_o) \, ds \end{aligned} \tag{6}$$

in which S_r denotes the surface occupied by the resistive sheet and S_o is the outer surface enclosing the volume V. As usual, $\hat{n}_r$ is the outward normal to S_r and $\hat{n}_o$ is correspondingly the outward normal to S_o. If S_r borders the outer surface of the volume V, then S_o should be considered to be just over the exterior side of S_r (i.e., S_o always encloses S_r).

Having derived the explicit form of the functional F, we may now expand the element field using the standard linear shape functions. If the sources are within V then F should be modified to read

$$\begin{aligned} F &= \int\int\int_V \left\{ \frac{1}{\mu_r}(\nabla \times \mathbf{E}) \cdot (\nabla \times \mathbf{E}) - k_o^2 \epsilon_r \mathbf{E} \cdot \mathbf{E} \right\} dv \\ &+ \int\int\int_V \mathbf{E} \cdot \left[jk_o Z_o \mathbf{J}^{int} - \nabla \times \left(\frac{1}{\mu_r} \mathbf{M}^{int} \right) \right] dv \\ &+ jk_o Z_o \int\int_{S_r} \frac{1}{R} (\hat{n}_r \times \mathbf{E}) \cdot (\hat{n}_r \times \mathbf{E}) ds \\ &+ jk_o Z_o \oiint_{S_o} \mathbf{E} \cdot (\mathbf{H} \times \hat{n}_o) ds \end{aligned} \tag{7}$$

where $(\mathbf{J}^{int}, \mathbf{M}^{int})$ denote the impressed sources internal to V. Then, upon setting the first order variation of F to zero, we can obtain a system of equations for the solution of the interior and boundary electric fields. For a unique solution of this system we must, however, specify a relation between the tangential electric and magnetic field which appear in the surface integral over S_o. If we assume that the subject volume is that occupied by the metal-backed cavity recessed in a ground plane, as shown in figure 2, then S_o reduces to the aperture area in that cavity. By invoking image theory, the magnetic field on the aperture can then be expressed as

$$\mathbf{H} = \mathbf{H}^{inc} + \mathbf{H}^{ref} - 2jk_o Y_o \int\int_{S_a} \left[\left(\bar{\mathbf{I}} + \frac{1}{k_o^2} \nabla\nabla \right) G_o(\mathbf{r}, \mathbf{r}') \right] \cdot [\mathbf{E}(\mathbf{r}) \times \hat{z}] \, ds' \tag{8}$$

where S_a denotes the aperture surface, $G_o(\mathbf{r}, \mathbf{r}')$ is the free space scalar Green's function, $\mathbf{r}$ specifies the observation point located on S_a and $\bar{\mathbf{I}} = \hat{x}\hat{x} + \hat{y}\hat{y} + \hat{z}\hat{z}$ is the unit dyad. Also, $\mathbf{H}^{inc}$ denotes the magnetic field generated by sources in the free space and $\mathbf{H}^{ref}$ is the corresponding reflected field

when the cavity's aperture is shorted. Substituting (8) into (7) gives a functional only in terms of the electric field. The system obtained from this functional will be partly sparse and partly full. In particular the volume integrals and that over S_r in (7) lead to a sparse submatrix involving the interior fields of the cavity. However, in view of (8) the last surface integral of (7) over S_o (or S_a) renders a full Toeplitz submatrix since the boundary integral is convolutional. Consequently, by resorting to an iterative solution such as the conjugate or biconjugate gradient method in conjunction with the fast Fourier transform, the need to generate the Toeplitz matrix is eliminated thus maintaining the O(n) storage requirement, characteristic of finite element solutions. The details pertaining to this implementation are discussed in [6] - [8]. In the next section we only present some results aimed at evaluating the accuracy of the proposed resistive sheet model.

3 Numerical Results

Let us consider the metal-backed rectangular cavity illustrated in Figure 2. The cavity is assumed to be empty (no internal sources) and is illuminated by a plane wave in the $\phi = 0$ plane. For implementing the aforementioned solution, the cavity is subdivided into rectangular bricks and the results of the solution are shown in Figure 3. These are radar cross section (RCS) patterns and refer to a 1λ deep cavity whose aperture is also $1\lambda \times 1\lambda$. The RCS pattern in Figure 3(b) applies to the cavity which is loaded with a resistive sheet of $100\Omega/\square$ placed at its aperture, whereas the result in Figure 3(b) is for the untreated empty cavity. The simulation of the resistive sheet was done through direct discretization of the first order variation of the functional F as given in (7) and alternatively by modeling the resistive sheet as a dielectric layer of thickness $\lambda/20$ having the dielectric constant computed from (2). As shown in Figure 3(b) the results based on the two simulations are in reasonable agreement and the differences among them is due to the finite thickness which was necessarily introduced in the physical model of the resistive sheet. As noted in [9] and [10], the dielectric layer introduces vertical components of the electric field which are not present in the resistive sheet. It is certainly of interest to point out that the presence of the resistive sheet at the aperture surface reduced the RCS of the cavity

by 10dB at normal incidence and by as much as 20dB at grazing incidence.

The second geometry which was considered is a circular metal-backed cavity again situated in a ground plane. In this case the aperture of the circular cavity is loaded with a sheet having non-uniform resistivity given by

$$R(\rho) = \begin{cases} Z_o \left[0.1 + 10\left(\frac{a-\rho}{a}\right)^2\right] & \rho > 0.5a \\ \\ \infty & \text{elsewhere on } S_a \end{cases}$$

where a denotes the radius of the aperture. Results with and without resistive loading for a cavity having a = 1in and a depth of 0.25in are shown in Figure 4. These RCS patterns were computed at 16GHz and the incident field is a plane wave in the xy plane polarized along the θ or ϕ direction. Again, the data in Figure 4 demonstrate the validity of the proposed mathematical model. Also, as in the case of the rectangular cavity the presence of the resistive cards causes substantial reduction in the overall RCS of the cavity. A vector map of the real and imaginary parts of the aperture electric fields is presented in Figure 5 generated with and without the resistive loading. This clearly demonstrates that the primary reason for the RCS reduction is due to the reduced strength of the electric fields normal to the rim of the circular cavity.

4 Conclusions

A formulation was derived for modeling resistive cards within the context of the finite element method. Essentially, the pertinent variational functional was supplemented with an additional boundary integral over the surface of the resistive sheet/card. Results based on the discretization of the functional were also presented aimed at demonstrating the accuracy of the derived mathematical model.

References

[1] T.B.A. Senior, "Scattering by Resistive Strips," *Radio Science*, Vol. 14, pp. 911-924, 1979.

[2] M.I. Herman and J.L. Volakis, "High Frequency Scattering by a Resistive Strip and Extensions to Conductive and Impedance Strips," *Radio Science*, Vol. **22**, pp. 335-349, May-June 1987.

[3] E.F. Knott and T.B.A. Senior, "Non-Specular Radar Cross Section Study," University of Michigan Radiation Laboratory Technical Report 011764-1-T (also U.S. Air Force Avionics Lab. report AFAL-TR-73-422) January 1974.

[4] R.F. Harrington and J.R. Mautz, "An Impedance Sheet Approximation for Thin Dielectric Shells," *IEEE Trans. Antennas Propagat.*, Vol. **AP-23**, pp. 531-534, 1975.

[5] T.B.A. Senior, "Combined Resistive and Conductive Sheets," *IEEE Trans. Antennas Propagat.*, Vol. **AP-33**, pp. 577-579, 1985.

[6] J.M. Jin and J.L. Volakis, "A Finite Element-Boundary Integral Formulation for Scattering by Three-Dimensional Cavity-Backed Apertures," *IEEE Trans. Antennas Propagat.*, Vol. **AP-39**, pp. 97-104, January 1991.

[7] J.M. Jin and J.L. Volakis, "Electromagnetic Scattering by and Transmission Through a Three-Dimensional Slot in a Thick Conducting Plane," *IEEE Trans. Antennas Propagat.*, Vol. **AP-39**, pp. 543-550, April 1991.

[8] J.M. Jin and J.L. Volakis, "Scattering and Radiation From Microstrip Patch Antennas and Arrays Residing in a Cavity," submitted to *IEEE Trans. Antennas Propagat.*.

[9] T.B.A. Senior and J.L. Volakis, "Sheet Simulation of Dielectric Layers," *Radio Science*, **22**, Dec. 1987, pp. 1261-1272.

[10] J.L. Volakis, "Numerical Implementation of Generalized Impedance Boundary Conditions," 1989 URSI Electromagnetic Theory Symposium, Aug. 1989, Stockholm, Sweden. Symposium Digest pp. 434-437.

FIGURE CAPTIONS

Fig. 1 Illustration of a dielectric volume in the presence of a resistive card. (a) Resistive card within the dielectric (b) Resistive card on the surface of the dielectric.

Fig. 2 Illustration of a cavity backed aperture in a ground plane.

Fig. 3 Monostatic RCS for a rectangular aperture ($1\lambda \times 1\lambda$) backed by a rectangular cavity ($1\lambda \times 1\lambda \times 1\lambda$) in the $\phi=0$ plane. (a) Empty cavity without resistive loading (b) Empty cavity whose aperture is covered with a resistive sheet having a resistivity of $100\Omega/\square$. (Solid and dashed lines correspond to results based on the mathematical simulation; circles and squares refer to results based on the physical modeling of the resistive sheet)

Fig. 4 Monostatic RCS for a circular aperture (1 inch in diameter) backed by a circular cavity (1 inch in diameter and 0.25 inches deep) at 16 GHz. (a) Empty cavity. (b) Empty cavity covered with a resistive sheet whose resistivity is given by equ. (12). (Solid and dashed lines correspond to results based on the mathematical simulation; circles and squares refer to results based on the physical modeling of the resistive sheet)

Fig. 5 Vector map of the electric field on the aperture of the circular cavity whose RCS is given in Fig. 4. (a) Empty cavity (b) Empty cavity covered with a resistive sheet whose resistivity is given by equ. (12).

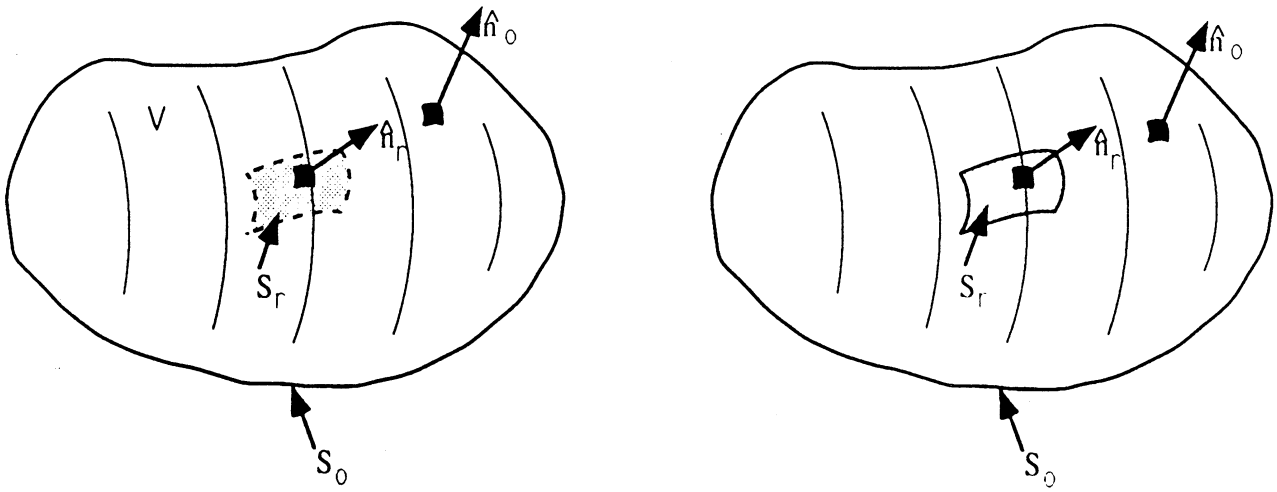

(a) (b)

Figure 1

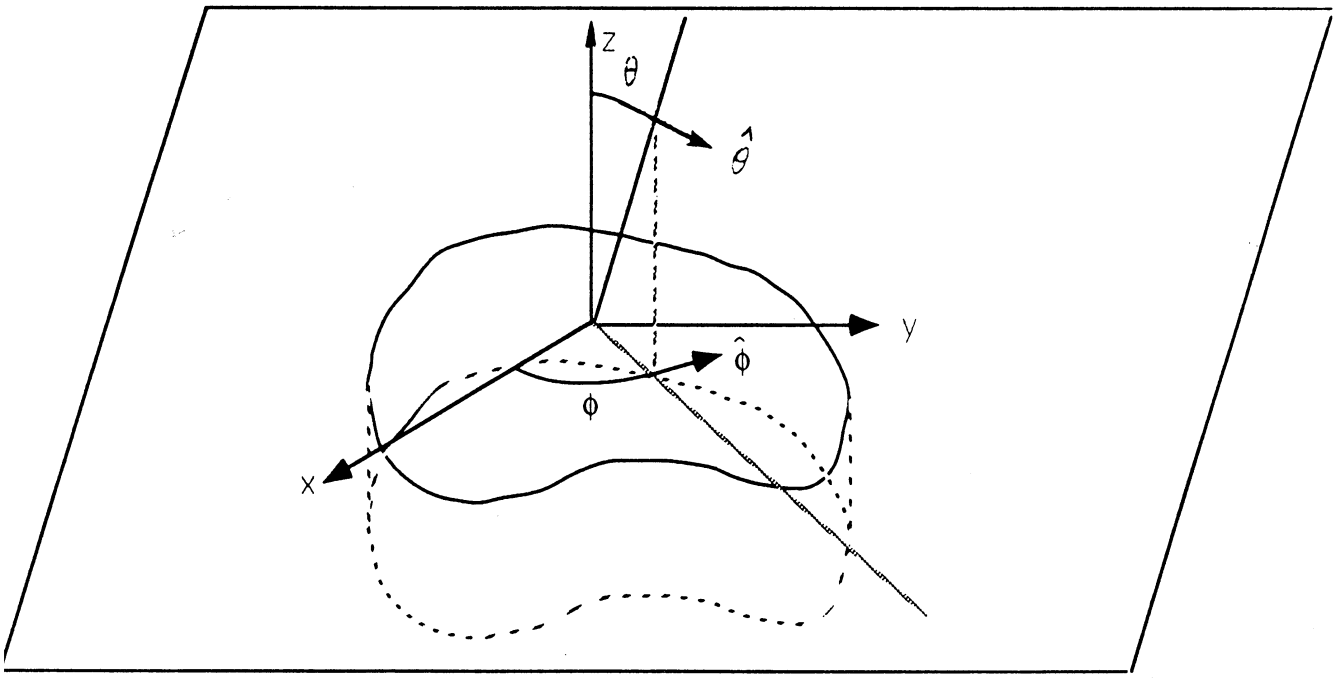

Figure 2

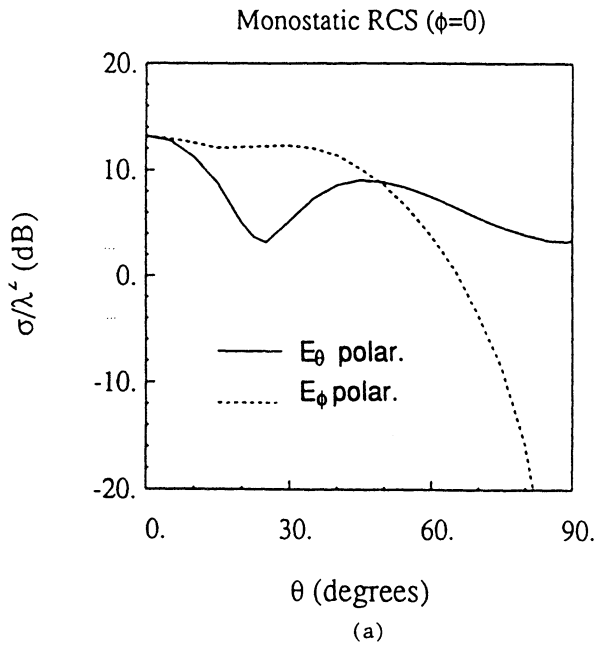

(a)

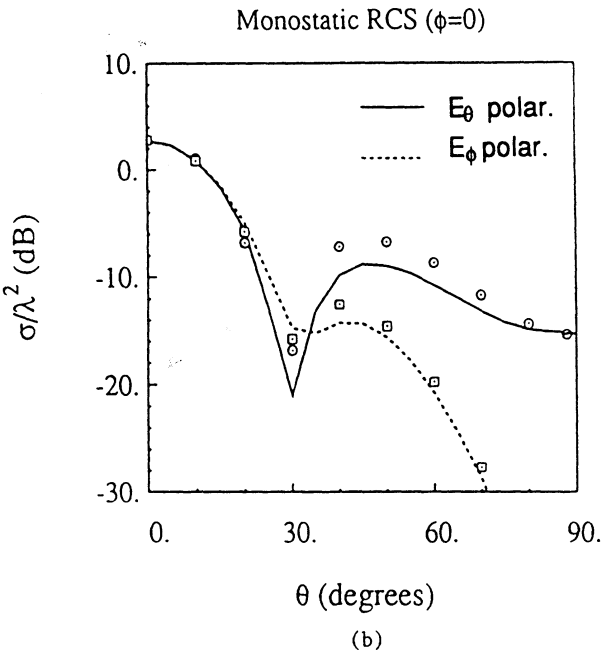

(b)

Figure 3

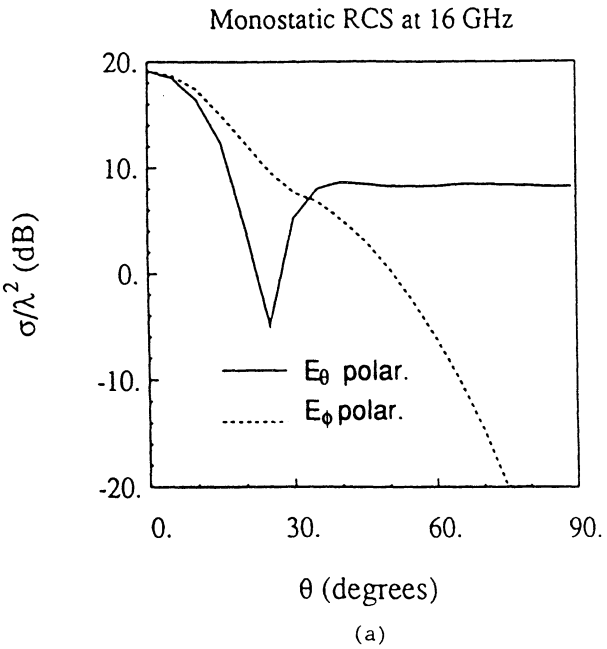

(a)

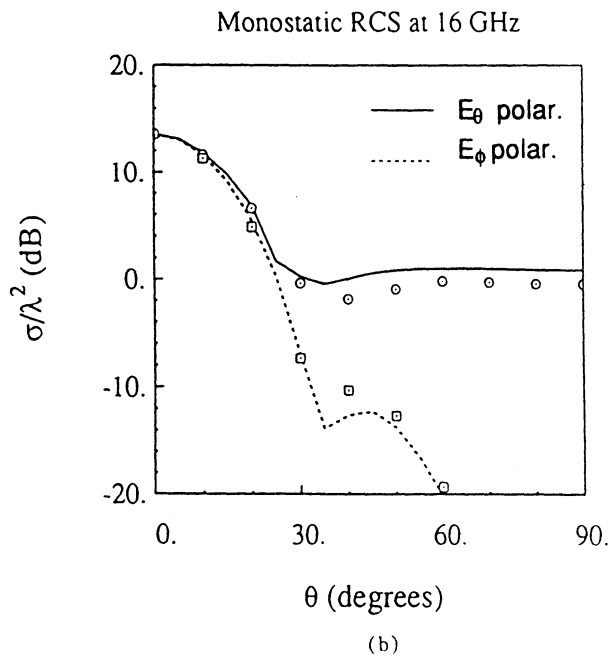

(b)

Figure 4

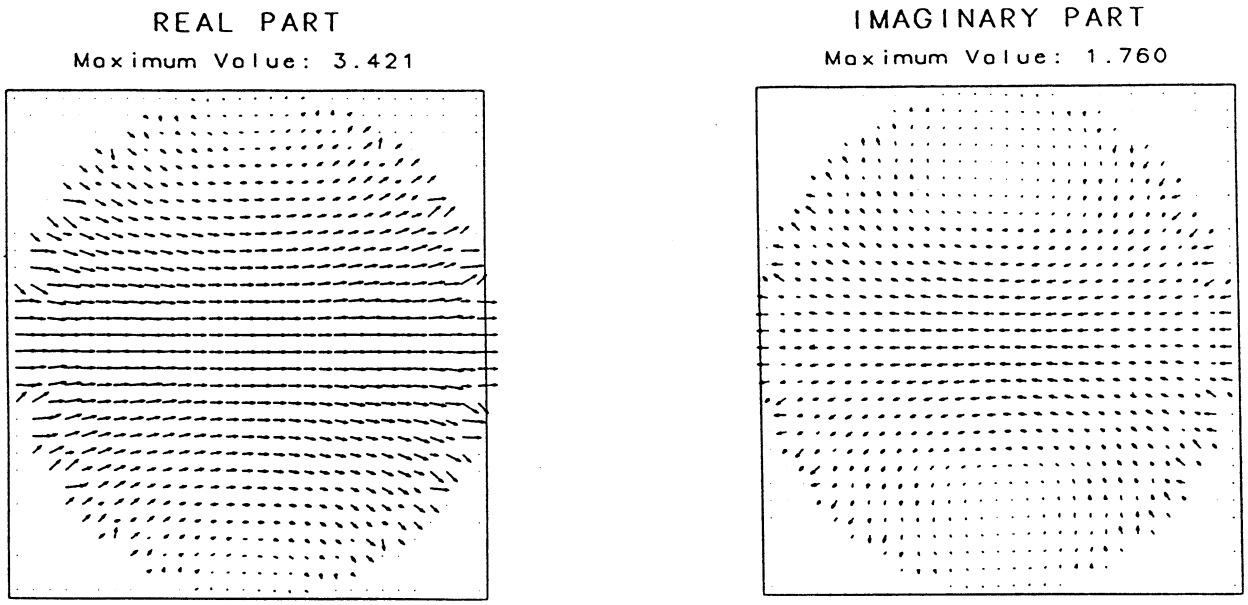
REAL PART
Maximum Value: 3.421
IMAGINARY PART
Maximum Value: 1.760

(a)

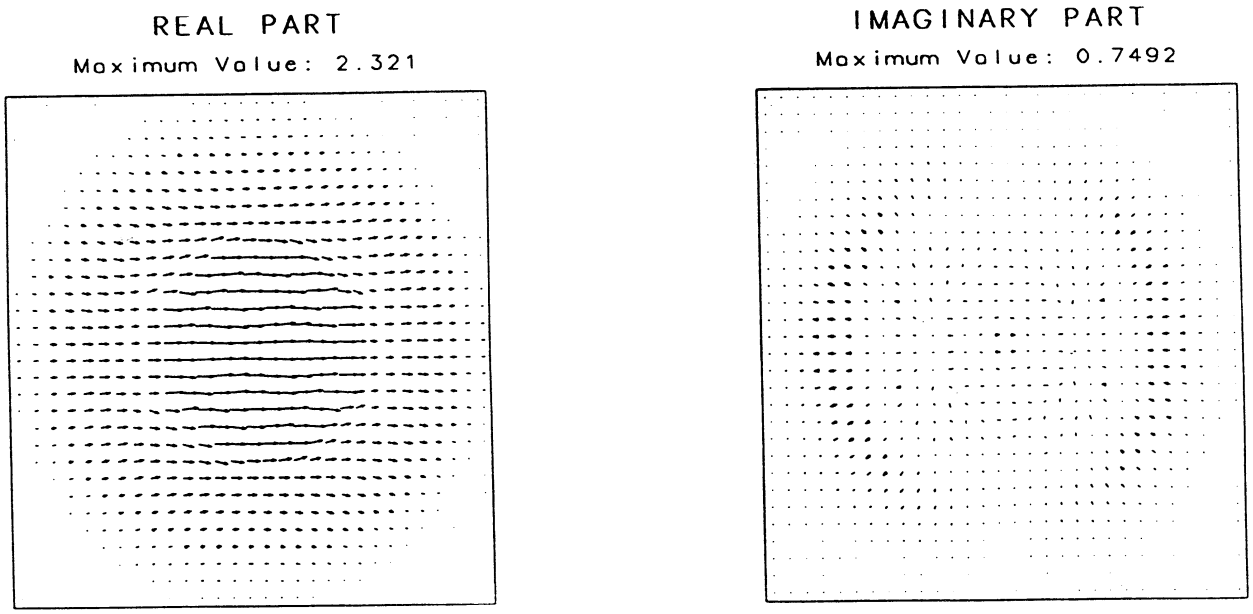
REAL PART
Maximum Value: 2.321
IMAGINARY PART
Maximum Value: 0.7492

(b)

Figure 5

UNIVERSITY OF MICHIGAN
3 9015 02229 1127